

# Earth and Space Science



## RESEARCH ARTICLE

10.1029/2022EA002778

This article is a companion to Nowlan et al. (2023), <https://doi.org/10.1029/2022EA002643>.

### Key Points:

- Monthly mean OMPS-NPP/N20 HCHO products have good agreement with Fourier-Transform Infrared observations, showing correlation coefficients of 0.83 and 0.88
- The smaller pixel sizes of OMPS-N20 as compared with OMPS-NPP can help detect pollution sources on small scales
- The relative uncertainty of OMPS-NPP (N20) HCHO monthly means is 31 (18)% with a bias of  $-15\% \pm 4\%$  ( $0.5\% \pm 6\%$ ) in high HCHO vertical column densities

### Supporting Information:

Supporting Information may be found in the online version of this article.

### Correspondence to:

H.-A. Kwon,  
[hakwon@suwon.ac.kr](mailto:hakwon@suwon.ac.kr)

### Citation:






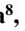



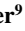









Kwon, H.-A., Abad, G. G., Nowlan, C. R., Chong, H., Souri, A. H., Vigouroux, C., et al. (2023). Validation of OMPS Suomi NPP and OMPS NOAA-20 formaldehyde total columns with NDACC FTIR observations. *Earth and Space Science*, 10, e2022EA002778. <https://doi.org/10.1029/2022EA002778>

Received 6 DEC 2022  
Accepted 12 APR 2023

### Author Contributions:

**Conceptualization:** H.-A. Kwon, G. González Abad

## Validation of OMPS Suomi NPP and OMPS NOAA-20 Formaldehyde Total Columns With NDACC FTIR Observations

H.-A. Kwon<sup>1,2</sup> , G. González Abad<sup>1</sup> , C. R. Nowlan<sup>1</sup> , H. Chong<sup>1</sup>, A. H. Souri<sup>1,3,4</sup> , C. Vigouroux<sup>5</sup> , A. Röhlings<sup>6</sup> , R. Kivi<sup>7</sup> , M. Makarova<sup>8</sup>, J. Notholt<sup>9</sup> , M. Palm<sup>9</sup> , H. Winkler<sup>9</sup> , Y. Té<sup>10</sup> , R. Sussmann<sup>11</sup>, M. Rettinger<sup>11</sup>, E. Mahieu<sup>12</sup>, K. Strong<sup>13</sup> , E. Lutsch<sup>13</sup> , S. Yamanouchi<sup>13</sup> , T. Nagahama<sup>14</sup>, J. W. Hannigan<sup>15</sup> , M. Zhou<sup>16</sup> , I. Murata<sup>17</sup>, M. Grutter<sup>18</sup> , W. Stremme<sup>18</sup>, M. De Mazière<sup>5</sup>, N. Jones<sup>19</sup> , D. Smale<sup>20</sup>, and I. Morino<sup>21</sup> 

<sup>1</sup>Center for Astrophysics, Harvard & Smithsonian, Cambridge, MA, USA, <sup>2</sup>Now at the University of Suwon, Gyeonggi-do, Republic of Korea, <sup>3</sup>Now at NASA Goddard Space Flight Center, Greenbelt, MA, USA, <sup>4</sup>Now at Morgan State University, Baltimore, MA, USA, <sup>5</sup>Royal Belgian Institute for Space Aeronomy (BIRA-IASB), Brussels, Belgium, <sup>6</sup>Karlsruhe Institute of Technology (KIT), IMK-ASF, Karlsruhe, Germany, <sup>7</sup>Finnish Meteorological Institute (FMI), Sodankylä, Finland, <sup>8</sup>Atmospheric Physics Department, Saint Petersburg State University, St. Petersburg, Russia, <sup>9</sup>Institute of Environmental Physics, University of Bremen, Bremen, Germany, <sup>10</sup>Laboratoire d'Études du Rayonnement et de la Matière en Astrophysique et Atmosphères (LERMA-IPSL), Sorbonne Université, CNRS, Observatoire de Paris, PSL Université, Paris, France, <sup>11</sup>Karlsruhe Institute of Technology (KIT), IMK-IFU, Garmisch-Partenkirchen, Germany, <sup>12</sup>Institut d'Astrophysique et de Géophysique, Université de Liège, Liège, Belgium, <sup>13</sup>Department of Physics, University of Toronto, Toronto, ON, Canada, <sup>14</sup>Institute for Space-Earth Environmental Research (ISEE), Nagoya University, Nagoya, Japan, <sup>15</sup>Atmospheric Chemistry, Observations & Modeling, National Center for Atmospheric Research (NCAR), Boulder, CO, USA, <sup>16</sup>Institute of Atmospheric Physics, Chinese Academy of Sciences (CAS), Beijing, China, <sup>17</sup>Graduate School of Environmental Studies, Tohoku University, Sendai, Japan, <sup>18</sup>Instituto de Ciencias de la Atmósfera y Cambio Climático, Universidad Nacional Autónoma de México (UNAM), Mexico City, México, <sup>19</sup>Centre for Atmospheric Chemistry, University of Wollongong, Wollongong, Australia, <sup>20</sup>National Institute of Water and Atmospheric Research Ltd (NIWA), Lauder, New Zealand, <sup>21</sup>National Institute for Environmental Studies, Tsukuba, Japan

**Abstract** We validate formaldehyde (HCHO) vertical column densities (VCDs) from Ozone Mapping and Profiler Suite Nadir Mapper (OMPS-NM) instruments onboard the Suomi National Polar-orbiting Partnership (Suomi NPP) satellite for 2012–2020 and National Oceanic and Atmospheric Administration-20 (NOAA-20) satellite for 2018–2020, hereafter referred to as OMPS-NPP and OMPS-N20, with ground-based Fourier-Transform Infrared (FTIR) observations of the Network for the Detection of Atmospheric Composition Change (NDACC). OMPS-NPP/N20 HCHO products reproduce seasonal variability at 24 FTIR sites. Monthly variability of OMPS-NPP/N20 has a very good agreement with FTIR, showing correlation coefficients of 0.83 and 0.88, respectively. OMPS-NPP (N20) biases averaged over all sites are  $-0.9 (4) \pm 3 (6)\%$ . However, at clean sites (with VCDs  $< 4.0 \times 10^{15}$  molecules  $\text{cm}^{-2}$ ), positive biases of  $20 (32) \pm 6 (18)\%$  occur for OMPS-NPP (N20). At sites with HCHO VCDs  $> 4.0 \times 10^{15}$  molecules  $\text{cm}^{-2}$ , negative biases of  $-15\% \pm 4\%$  appear for OMPS-NPP, but OMPS-N20 shows smaller bias of  $0.5\% \pm 6\%$  due to its smaller ground pixel footprints. Therefore, smaller satellite footprint sizes are important in distinguishing small-scale plumes. In addition, we discuss a bias correction and provide lower limit for the monthly uncertainty of OMPS-NPP/N20 HCHO products. The total uncertainty for OMPS-NPP (N20) at clean sites is  $0.7 (0.8) \times 10^{15}$  molecules  $\text{cm}^{-2}$ , corresponding to a relative uncertainty of 32 (30)%. In the case of HCHO VCDs  $> 4.0 \times 10^{15}$  molecules  $\text{cm}^{-2}$ , however, the relative uncertainty in HCHO VCDs for OMPS-NPP (N20) decreases to 31 (18)%.

**Plain Language Summary** Formaldehyde is a proxy for nonmethane volatile organic compounds (NMVOCs). Formaldehyde observations from satellites have been widely used to investigate NMVOC emissions, ozone production regime with  $\text{NO}_x$ , and the production of secondary organic aerosols. We validate new publicly available satellite formaldehyde observations from two Ozone Mapping and Profiler Suite (OMPS) instruments onboard Suomi NPP and NOAA-20 satellites, called OMPS-NPP and OMPS-N20 hereafter, with ground-based Fourier-Transform Infrared (FTIR) observations. OMPS-NPP/N20 products show good correlation coefficients of 0.83 and 0.88 compared to FTIR and also capture seasonal variability at 24 sites. However, OMPS products have a bias depending on formaldehyde concentrations. In low formaldehyde concentrations, positive biases of  $20 (32) \pm 6 (18)\%$  occur for OMPS-NPP (N20). In high

© 2023 The Authors.

This is an open access article under the terms of the [Creative Commons Attribution-NonCommercial License](https://creativecommons.org/licenses/by/4.0/), which permits use, distribution and reproduction in any medium, provided the original work is properly cited and is not used for commercial purposes.

**Data curation:** C. R. Nowlan, C. Vigouroux, A. Röhling, R. Kivi, M. Makarova, J. Notholt, M. Palm, H. Winkler, Y. Té, R. Sussmann, M. Rettinger, E. Mahieu, K. Strong, E. Lutsch, S. Yamanouchi, T. Nagahama, J. W. Hannigan, M. Zhou, I. Murata, M. Grutter, W. Stremme, M. De Mazière, N. Jones, D. Smale, I. Morino  
**Investigation:** H.-A. Kwon  
**Methodology:** H.-A. Kwon, G. González Abad, H. Chong, A. H. Souri  
**Writing – original draft:** H.-A. Kwon  
**Writing – review & editing:** H.-A. Kwon, G. González Abad, C. R. Nowlan, H. Chong, A. H. Souri, C. Vigouroux, R. Kivi, M. Makarova, J. Notholt, Y. Té, E. Mahieu, K. Strong, J. W. Hannigan, M. Grutter, N. Jones, I. Morino

concentrations, negative biases of  $-15\% \pm 6\%$  appear for OMPS-NPP, but OMPS-N20 products have a smaller bias of  $0.5\% \pm 6\%$  due to its smaller ground pixel footprints. This implies that smaller satellite footprint sizes are important in distinguishing small-scale plumes. In addition, we provide a lower limit for the monthly uncertainty of OMPS-NPP/N20 formaldehyde products.

## 1. Introduction

Ambient atmospheric formaldehyde (HCHO), produced by the oxidation of nonmethane volatile organic compounds (NMVOCs), is one of the most useful trace gases for investigating NMVOC emissions, ozone chemistry with  $\text{NO}_x$ , and the production of secondary organic aerosols (Liao et al., 2019; Marais et al., 2016; Schroeder et al., 2017; Souri et al., 2020; Travis et al., 2022). Such studies have used HCHO measured by in situ and remote sensing techniques and from various platforms such as satellites, aircraft, ships, and ground-based sites. HCHO satellite observations have been used to estimate NMVOC emissions in global and regional domains such as Asia, Europe, and the Americas, as Low Earth Orbit (LEO) satellites can cover the entire globe (Cao et al., 2018; Choi et al., 2022; Kaiser et al., 2018; Souri et al., 2021; Stavrou et al., 2015). HCHO airborne observations have been used to focus on local NMVOCs emissions (Fried et al., 2020; Kwon et al., 2021), and ship-based observations have been used to examine outflows from continents (Behrens et al., 2019). Ground-based observations such as Fourier-Transform Infrared (FTIR) and multi-axis differential optical absorption spectroscopy (MAX-DOAS) can be used to monitor pollution levels and trends and to validate satellite observations (De Smedt et al., 2021; Vigouroux et al., 2018, 2020).

Global HCHO satellite observations made from different platforms continue the data record that began with the Global Ozone Monitoring Experiment (GOME) on the ERS-2 LEO satellite in 1995 (Chance et al., 2000). The follow-on LEO satellite instruments Scanning Imaging Absorption Spectrometer for Atmospheric Cartography (SCIAMACHY), GOME-2A, GOME-2B, and GOME-2C have provided global HCHO data with morning overpass times at various spatial resolutions (De Smedt et al., 2008, 2012; Wittrock et al., 2006). Afternoon measurements began with observations from the Ozone Monitoring Instrument (OMI), launched in 2004 into an orbit with an equator crossing of  $\sim 13:30$  local time, and with a finer spatial resolution of  $13 \text{ km} \times 24 \text{ km}$  at nadir than previous instruments (De Smedt et al., 2015; González Abad et al., 2015). The Tropospheric Monitoring Instrument (TROPOMI) has collected HCHO observations with much finer spatial resolutions of  $7 \text{ km} \times 3.5 \text{ km}$  since 2018 ( $5.5 \text{ km} \times 3.5 \text{ km}$  since August 2019; De Smedt et al., 2018, 2021). The Environmental Monitoring Instrument on the Chinese GaoFen-5 satellite launched in May 2018 has provided additional HCHO observations in the afternoon (Su et al., 2022). Geostationary satellites can measure hourly variations of HCHO and fill a gap between morning and afternoon measurements from LEO satellites. The Geostationary Environment Monitoring Spectrometer, the first geostationary mission for trace gases, was launched in February 2020 and began measuring HCHO vertical columns  $\sim 8$  times per day, together with cloud properties, ozone, nitrogen dioxide, sulfur dioxide, aerosols, and health information such as ultraviolet (UV) index and vitamin D index (Bak et al., 2019; Go et al., 2020; Kang et al., 2020, 2022; G. Kim et al., 2021; J. Kim et al., 2020; M. Kim et al., 2018; Kwon et al., 2019; Park et al., 2021).

The Ozone Mapping and Profiler Suite Nadir Mapper (OMPS-NM) instruments onboard the Suomi National Polar-orbiting Partnership (Suomi NPP) and National Oceanic and Atmospheric Administration-20 (NOAA-20) satellites were launched in October 2011 and November 2017. Li et al. (2015) and González Abad et al. (2016) retrieved HCHO total columns from OMPS-NM observations onboard Suomi NPP with principal component analysis and hyperspectral direct fitting methods, respectively. Recently, we have developed updated, multiyear, and publicly available OMPS-NM HCHO products using hyperspectral direct fitting (González Abad, 2022a, 2022b; Nowlan et al., 2022). These OMPS-NM HCHO products can play an important role in augmenting and extending long-term HCHO data sets from OMI, since all three products share algorithms. Unfortunately, OMI has been affected by the row anomaly since 2008, reducing the frequency at which it achieves total coverage of the globe (Torres et al., 2018). OMPS-NM products can make up for a loss of pixels in OMI, allowing us to construct afternoon HCHO climatological data sets from 2004 until now with daily global coverage. Furthermore, NOAA plans to launch OMPS-NM instruments in successive operational satellites, which can provide a consistent set of HCHO observations starting in 2012 and extending to the 2030s. It is also worth considering that when TROPOMI is decommissioned NOAA OMPS-NM instruments will be the main source of HCHO observations in the afternoon overpass.

HCHO products of OMPS-NM onboard Suomi NPP produced by González Abad et al. (2016) have been validated using a model and aircraft observations. Souri et al. (2020) and Choi et al. (2022) found low biases of 20% and 37.5% in the OMPS-NM products, respectively, compared to model simulations during the Korea–United States Air Quality (KORUS-AQ) campaign. These studies focused only on South Korea and indirectly validated OMPS HCHO products using a model intercomparison platform, which corrects model concentrations by comparing observations from aircraft campaigns and uses the corrected model results to validate satellite observations (Zhu et al., 2020). Zhu et al. (2016) validated OMPS-NM HCHO measurements made over the southeast U.S. during the 2013 SEAC<sup>4</sup>RS (Studies of Emissions, Atmospheric Composition, Clouds and Climate Coupling by Regional Surveys) campaign and found OMPS-NM HCHO underestimated aircraft-corrected GEOS-Chem model columns by 34%.

In this study, we validate the updated OMPS-NM HCHO products with ground-based FTIR HCHO observations from the Network for the Detection of Atmospheric Composition Change (NDACC; De Mazière et al., 2018). Henceforth, we refer to OMPS-NM onboard Suomi NPP and NOAA-20 as OMPS-NPP and OMPS-N20, respectively. Section 2 describes OMPS-NPP/N20 HCHO products and FTIR HCHO products. The method for the comparison between OMPS-NPP/N20 and FTIR HCHO products is also described in this section. In Section 3, OMPS-NPP/N20 are validated with FTIR observations, and the importance of spatial pixel sizes is discussed for validation in heterogeneous scenes. OMPS-NPP/N20 uncertainties and biases as compared to FTIR observations are estimated in Section 4.

## 2. Data and Method

### 2.1. OMPS-NPP/N20 HCHO Observations

OMPS-NPP/N20 nadir mapper instruments measure backscattered radiances in the UV spectral range of 300–380 (420 for OMPS-N20) nm with a spectral resolution of  $\sim 1$  nm and a sampling of  $\sim 0.42$  nm, with a local overpass time of  $\sim 13:30$ . OMPS-NPP has a nadir pixel size of 50 km  $\times$  50 km, and OMPS-N20 has a finer pixel size of 17 km  $\times$  17 km, which is subsequently improved to 12 km  $\times$  17 km (since 13 February 2019) by trading off signal-to-noise ratio performance. The OMPS nadir mappers have been used to measure the global distribution and vertical profiles of ozone (Bak et al., 2017; Kramarova et al., 2014), sulfur dioxide (Li et al., 2017; Yang et al., 2013), nitrogen dioxide (Yang et al., 2014), and UV aerosol index (Torres, 2019).

OMPS-NPP/N20 HCHO vertical columns are obtained using the Smithsonian Astrophysical Observatory (SAO) retrieval algorithm (González Abad et al., 2016; Nowlan et al., 2022). The SAO algorithm was originally applied to GOME and has since been used to retrieve trace gases from OMI (González Abad et al., 2015). The algorithm also forms the basis for trace gas retrievals from the upcoming North American geostationary mission, Tropospheric Emissions: Monitoring of Pollution (TEMPO; Zoogman et al., 2017). It consists of spectral radiance fitting, an air mass factor (AMF) calculation, and bias/reference sector corrections. The radiance fitting derives differential slant column densities using direct intensity fitting, sometimes referred to as a basic optical absorption spectroscopy approach. AMFs are calculated using online radiative transfer calculations performed with VLIDORT version 2.8 (Spurr & Christi, 2019). The radiative transfer calculations use the Moderate Resolution Imaging Spectroradiometer bidirectional reflectance distribution function to determine surface reflectance and GEOS-Chem monthly mean climatological profiles, at the time of satellite overpass, for atmospheric composition. As a clean radiance reference over the remote Pacific is used as a reference spectrum in the radiance fitting, a reference sector correction (also called a background correction) is also conducted. A further bias correction is also conducted to correct for latitudinally dependent spectral correlations for ozone and bromine monoxide (BrO) distributions or other poorly understood latitudinally correlated artifacts that can be significant at low light levels. Nowlan et al. (2022) describe in detail the fitting parameters and retrieval steps used to derive OMPS-NPP and OMPS-N20 HCHO products.

In this study, OMPS-NPP/N20 HCHO products are used during 2012–2020/2018–2020, respectively, and only pixels with the following conditions are considered (Table 1): main data quality flag of zero, cloud fractions less than 0.4, solar zenith angle less than 70°, and snow/ice fraction of zero. Additionally, the median and median absolute deviation of the root mean square of fitting residuals are used to filter out outlier pixels, where the radiance fitting converges but fitting residuals are anomalously high.

### 2.2. FTIR HCHO Observations

We use harmonized NDACC FTIR HCHO observations. To minimize possible biases between the various sites, NDACC FTIR enforces the harmonized retrieval settings including a consistent spectroscopic database and

**Table 1**  
*Summary of OMPS-NPP/N20 Data Filtering and Matching Criteria to Build Comparable Data Sets*

OMPS-NPP/N20 data filtering criteria	
Main data quality flag	=0
Cloud fraction	<0.4
Solar zenith angle	<70
Root mean square (RMS) of fitting residuals	<Median(RMS) + MAD(RMS)
Matching criteria to build comparable data sets	
The minimum number of pixels for OMPS-NPP and N20	10 and 90
A sampling spatial grid (°)	0.5
A sampling time window (hr)	±3

*Note.* MAD is the median absolute deviation converted to  $1\sigma$  standard deviation for normal distributions with a factor of  $k = 1.4826$ .

fitting window (Vigouroux et al., 2018). NDACC FTIR groups use two retrieval codes: SFIT4 and PROFFIT, and the two codes produce very consistent retrieval products according to a previous comparison study by Hase et al. (2004). The details of the harmonized retrievals for FTIR are given in Vigouroux et al. (2018).

Table 2 summarizes NDACC FTIR locations, retrieval codes, institutes of the principal investigators, observation periods, and geographical region. Three Arctic sites (Eureka, Ny-Ålesund, and Thule) are excluded in our analysis, as compared to Vigouroux et al. (2020). Current cloud fraction information used in OMPS-NPP/N20 products is invalid over snow and ice and set at a value of either 0 or 1. Therefore, most satellite pixels over those Arctic sites are filtered out due to unrealistic cloud information over snow and ice. If future OMPS-NPP/N20 algorithms implement improved cloud retrievals over snow and ice, OMPS-NPP/N20 can be validated in Arctic regions. Two sites (Karlsruhe and Saint-Denis on the island of Réunion) have been included in the harmonized NDACC FTIR HCHO network since Vigouroux et al. (2020).

Figure 1 shows NDACC FTIR sites over a global map of OMPS-NPP HCHO vertical column densities (VCDs). NDACC FTIR locations cover a range of HCHO columns, from clean oceanic regions to polluted regions influenced by biogenic and anthropogenic sources of VOCs, and from the Northern to the Southern Hemisphere. Therefore, NDACC FTIR observations provide the opportunity to examine and validate satellite observations over a variety of regions and conditions.

### 2.3. Construction of Comparable Data Sets

To compare satellite and ground-based observations, we need to collect high-quality data and then build comparable pairs, which are spatially and temporally collocated. First, we collect OMPS-NPP/N20 pixels with the quality control conditions mentioned in Section 2.1. Then, satellite and ground-based observations need to be spatially and temporally collocated. For OMPS-NPP, the median of the fitting uncertainties is  $\sim 3.5 \times 10^{15}$  molecules  $\text{cm}^{-2}$  over the reference sector in June 2018, and several pixels need to be averaged to reduce noise and match the precision of the ground-based observations. Vigouroux et al. (2020) showed that the median uncertainty related to random components for FTIR observations was  $2.3 \times 10^{14}$  molecules  $\text{cm}^{-2}$ , which is  $\sim 10$  times lower than that of OMPS-NPP. Therefore, at least 100 OMPS-NPP pixels ideally need to be combined to bring OMPS-NPP precision to FTIR levels.

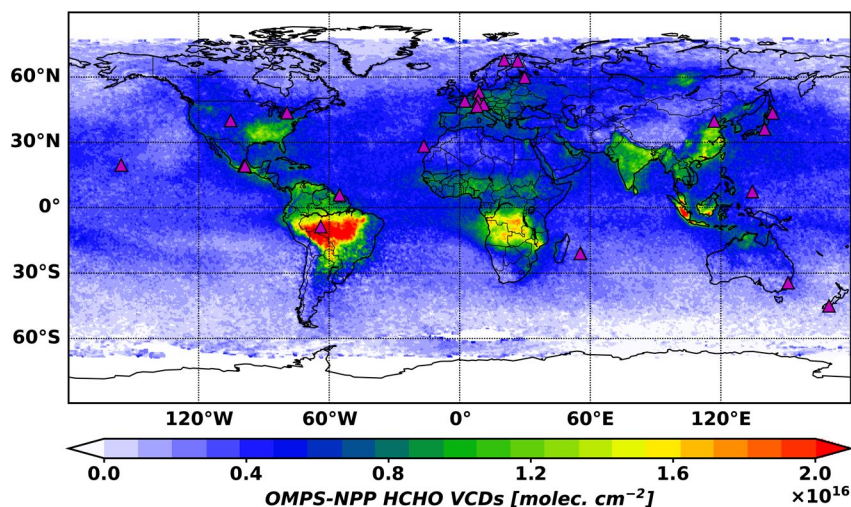
For this study, we take monthly averaged pairs for the comparison between satellites and ground-based observations to reduce noise of satellite observations but still keep monthly temporal resolution for long-term time series. Although OMPS-NPP monthly means have lower precision than FTIR measurements due to fewer sampling pixels than 100 on average ( $\sim 40$  sampling pixels per a pair), we can validate the performance of satellite monthly means, which have been used in application studies. However, given OMPS-NPP pixel sizes and coincident observations between OMPS and FTIR, some cases can occur where only a few pixels are used for a monthly mean. In consequence, to ensure robust statistics, we use comparable pairs where at least 10 pixels from OMPS-NPP



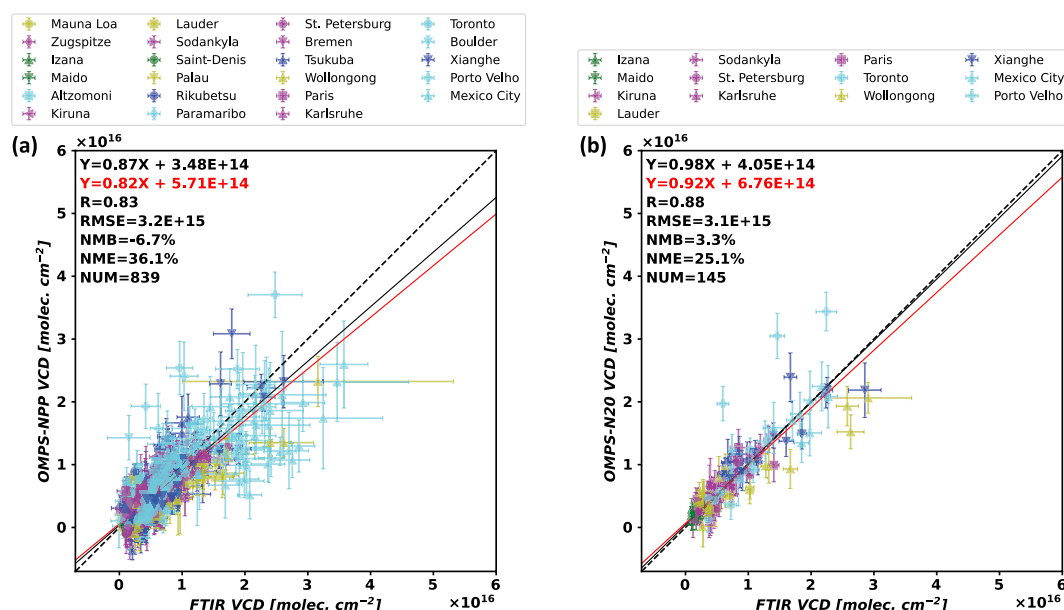
**Table 2**  
Summary of NDACC FTIR Sites

Station	Latitude, longitude	Altitude (km)	Code	Institute	Time coverage	Continent/ocean	Color in figures <sup>a</sup>
Kiruna	67.84°N, 20.40°E	0.42	PROFFIT	KIT-ASF; IRF Kiruna	01/2005 to 11/2019	Europe	Magenta
Sodankylä <sup>b</sup>	67.37°N 26.63°E	0.19	SFIT4	FMI; BIRA	03/2012 to 04/2020	Europe	
St. Petersburg	59.88°N, 29.83°E	0.02	SFIT4	SPbU	03/2009 to 08/2019	Europe	
Bremen	53.10°N, 8.85°E	0.03	SFIT4	U. of Bremen	10/2004 to 12/2019	Europe	
Karlsruhe <sup>b</sup>	49.10°N, 8.42°E	0.11	PROFFIT	KIT-ASF	02/2018 to 05/2020	Europe	
Paris <sup>b</sup>	48.85°N, 2.36°E	0.06	PROFFIT	Sorbonne U.	03/2011 to 08/2019	Europe	
Zugspitze	47.42°N, 10.98°E	2.95	PROFFIT	KIT-IFU	03/1995 to 06/2020	Europe	
Jungfrauoch	46.55°N, 7.98°E	3.58	SFIT4	U. of Liege	01/2017 to 01/2020	Europe	
Maïdo	21.08°S, 55.38°E	2.16	SFIT4	BIRA	03/2013 to 12/2019	Africa and Indian Ocean	Green
Saint-Denis	20.9°S, 55.49°E	0.85	SFIT4	BIRA	08/2004 to 06/2015	Africa and Indian Ocean	
Izaña	19.54°N, 155.57°W	2.37	PROFFIT	AEMET; KIT-ASF	01/2005 to 12/2019	Africa	
Toronto	43.60°N, 79.36°W	0.174	SFIT4	U. of Toronto	05/2002 to 12/2019	North America	Cyan
Boulder	40.04°N, 105.24°W	1.61	SFIT4	NCAR	04/2010 to 12/2019	North America	
Mexico City <sup>b</sup>	19.33°N, 99.18°W	2.26	PROFFIT	UNAM	01/2013 to 10/2019	North America	
Altzomoni	19.12°N, 98.66°W	3.99	PROFFIT	UNAM	09/2012 to 09/2019	North America	
Paramaribo	5.81°N, 55.21°W	0.03	SFIT4	U. of Bremen	09/2004 to 05/2020	South America	
Porto Velho <sup>b</sup>	8.77°S, 63.87°W	0.09	SFIT4	BIRA	07/2016 to 12/2019	South America	
Rikubetsu	43.46°N, 143.77°E	0.38	SFIT4	Nagoya U.; NIES	05/1995 to 12/2019	Asia	Blue
Xianghe <sup>b</sup>	39.75°N, 116.96°E	0.05	SFIT4	CAS; BIRA	06/2018 to 02/2020	Asia	
Tsukuba <sup>b</sup>	36.05°N, 140.12°E	0.03	SFIT4	NIES; Tohoku U.	05/2001 to 12/2019	Asia	
Mauna Loa	19.54°N, 155.57°W	3.40	SFIT4	NCAR	08/1995 to 12/2019	Pacific Ocean	Yellow
Palau <sup>b</sup>	7.34°N, 134.47°E	0.03	SFIT4	U. of Bremen	03/2019 to 05/2020	Oceania	
Wollongong	34.41°S, 150.88°E	0.03	SFIT4	U. of Wollongong	05/1996 to 01/2020	Oceania	
Lauder	45.04°S, 169.68°E	0.37	SFIT4	NIWA	10/2001 to 12/2019	Oceania	

<sup>a</sup>Figures 2 and 3. <sup>b</sup>The sites are not officially affiliated to NDACC.



**Figure 1.** A global map of OMPS-NPP HCHO mean vertical column densities at a horizontal resolution of  $0.5^\circ \times 0.5^\circ$  in September 2012. Triangle marks in magenta denote Fourier-Transform Infrared (FTIR) observation sites.



**Figure 2.** Scatter plots (a) between OMPS-NPP and Fourier-Transform Infrared (FTIR) data (2012–2020) and (b) between OMPS-N20 and FTIR data (2018–2020) for monthly mean comparable pairs. Black and red lines are regression lines from the reduced major axis method not weighted with uncertainties and the bivariate method weighted with uncertainties, respectively. The slopes and  $y$ -intercepts are given in each panel. A correlation coefficient ( $R$ ), root mean square error (RMSE), normalized mean bias (NMB), normalized mean error (NME), and the number of pairs (NUM) are given in each panel. Colors of symbols indicate the region classification of sites shown in Table 2.

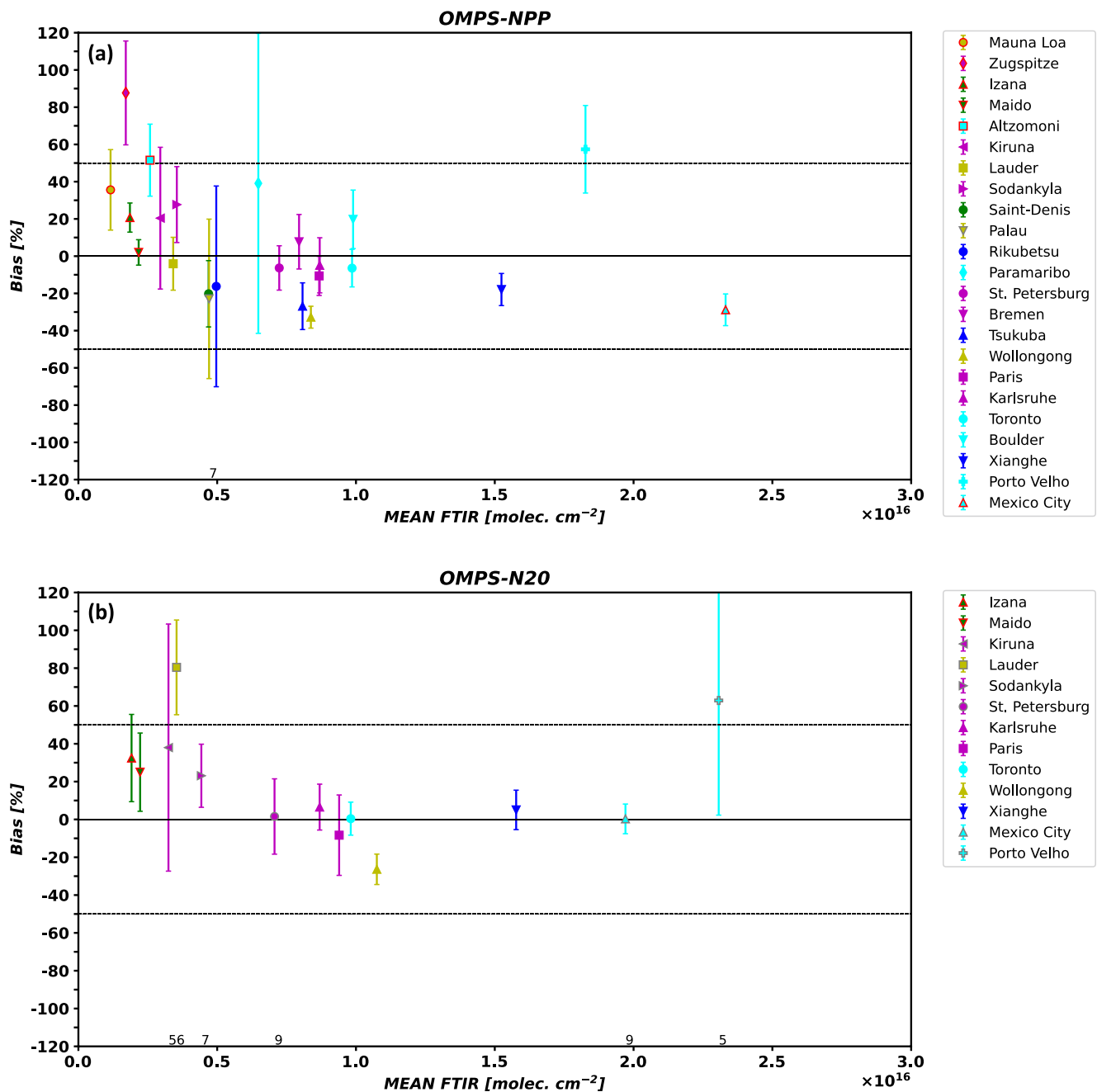
can be collected for a monthly mean. Also, sites are considered only if five or more monthly pairs are available to ensure meaningful statistics.

The OMPS-N20 instrument is nearly identical to OMPS-NPP but its binned spectra result in  $\sim 9$  times finer footprints (based on a nadir pixel size of  $17 \text{ km} \times 17 \text{ km}$ ), leading to about 3 times lower precisions of  $9.6 \times 10^{15}$  molecules  $\text{cm}^{-2}$ . Thus, we use 9 times more pixels (making it at least 90 pixels) for OMPS-N20 owing to its smaller pixels size and low signal-to-noise ratio to satisfy the same precision with OMPS-NPP in the comparisons.

To collect enough satellite pixels while maintaining spatial coincidence, it is necessary to choose proper spatial ranges. OMPS-NPP has pixel sizes of roughly  $50 \text{ km} \times 50 \text{ km}$  across most of the swath, which increase rapidly to several hundred km in the cross-track direction near the edge of the swath. We test grid sizes of  $0.2^\circ$  and  $0.5^\circ$  with the center located at the latitude and longitude coordinates of FTIR stations for sampling pixels, considering FTIR data collected  $\pm 3$  hr from the satellite observation. The selection of both spatial grid and temporal window has to ensure that enough pixels are collocated. In the case of a  $0.2^\circ$  spatial grid, the numbers of collocated pixels for OMPS-N20 do not satisfy the minimum number of 90 pixels at half of the sites. Therefore, we choose the grid size of  $0.5^\circ$  to maximize the information available for both OMPS-NPP and N20 (Table 1).

Vigouroux et al. (2020) noted that FTIR observations occurred with a frequency of 3–10 per day. Also, they pointed out that a short time window could reduce the number of comparable pairs and that a longer time window could exacerbate the effects of the diurnal variation of HCHO. To find an optimal time window, we conduct the sensitivity test of time windows of  $\pm 3$  and  $\pm 6$  hr with a spatial coadding grid of  $0.5^\circ$ . A time window of  $\pm 6$  hr increases the number of comparable pairs, but the normalized mean error (NME),  $\frac{\sum |OMPS - FTIR|}{\sum FTIR}$ , rarely changes compared to results using  $\pm 3$  hr. Therefore, to reduce the impact of diurnal cycles on comparable pairs, a time window of  $\pm 3$  hr is used (Table 1). Keeping in mind that OMPS-NPP/N20 local overpass time is  $\sim 13:30$  at nadir, we consider FTIR observations between 10:30 and 16:30 local time.

We minimize the effects of a priori profiles and averaging kernels (AKs) on the comparison between OMPS-NPP/N20 and FTIR observations following the Vigouroux et al. (2020) methodology. The OMPS-NPP/N20 products use a priori profiles from GEOS-Chem, while the NDACC FTIR products use a single profile from the Whole Atmosphere Community Climate Model (WACCM) at each site. For consistency, a priori profiles from OMPS-NPP/N20 are interpolated to the FTIR vertical grid, considering mass conservation (Langerock



**Figure 3.** Biases (%) (a) between OMPS-NPP and Fourier-Transform Infrared (FTIR) data and (b) between OMPS-N20 and FTIR data at each site. Sites with the number of monthly mean pairs greater than 4 are plotted. The number of the comparable pairs less than 10 is provided at the bottom of the figures. Error bars indicate the errors of the biases, and colors of symbols indicate the region classification of sites shown in Table 2. Red and gray edges of symbols indicate high-altitude sites and the number of the comparable pairs less than 10, respectively.

et al., 2015), and then are applied using the method of Rodgers and Connor (2003) and Vigouroux et al. (2020) to calculate the retrieved FTIR profiles with the a priori profile correction. To directly compare FTIR and OMPS results, the corrected FTIR profiles are interpolated on OMPS-NPP/N20 vertical grids and smoothed with AKs from OMPS-NPP/N20 using the approach described in Rodgers and Connor (2003) and Vigouroux et al. (2020). Also, a scale factor is used to consider surface elevations based on FTIR locations (Vigouroux et al., 2020).

As mentioned above, we use monthly averaged pairs for satellite- and ground-based observations. For OMPS-NPP/N20, the weighted mean of individual pixels is calculated using the ratio of the area of a grid cell covered by each satellite pixel ( $A$ ) to the area of individual pixels ( $A^p$ ) as a weighting. FTIR observations spatially and temporally

collocated with OMPS-NPP/N20 pixels are also averaged with the same weights at each OMPS-NPP/N20 pixel. For the seasonal variability, all OMPS-NPP/N20 pixels are used during the observation periods of each site.

A standard uncertainty of the weighted mean ( $\sigma_w$ ) is calculated with an equation from Gatz and Smith (1995) as follows:

$$\sigma_w^2 = \frac{n}{(n-1)(n\bar{w})} \left( \sum_{i=1}^n (w_i x_i - \bar{w} \bar{x}_w)^2 - 2\bar{x}_w \sum_{i=1}^n (w_i - \bar{w})(w_i x_i - \bar{w} \bar{x}_w) + \bar{x}_w^2 \sum_{i=1}^n (w_i - \bar{w})^2 \right), \quad (1)$$

where  $n$  is the number of comparable pairs,  $w_i$  and  $x_i$  are the weighting factor ( $A_i/A_i^p$ ) and OMPS-NPP/N20 or FTIR HCHO VCD of comparable pair  $i$ , respectively,  $\bar{w}$  is an arithmetic mean for the weighting factors, and  $\bar{x}_w$  is the weighted mean of HCHO VCDs. Gatz and Smith (1995) validated the uncertainty from Equation 1 using a bootstrapping method, and the uncertainty was almost identical to the one from the bootstrapping method.

### 3. Results

#### 3.1. OMPS-NPP/N20 Validation With FTIR Observations

To validate OMPS-NPP/N20 HCHO VCDs, we use monthly mean comparable pairs with FTIR data as described in Section 2.3 and two bivariate least square methods: the reduced major axis (RMA) and a method from York et al. (2004) (called the York method). While the RMA method does not consider the uncertainty, the York method is a bivariate method weighted with uncertainties, which is likely a more reasonable approximation of the slope and y-intercept due to its consideration of uncertainties in both observations.

Figure 2 shows scatter plots between OMPS-NPP/N20 and FTIR observations with their uncertainty in Equation 1. Jungfraujoch is excluded in the scatter plot for OMPS-NPP because only 1 pair of 15 comparable pairs satisfied the minimum number of 10 pixels for monthly mean pairs. Likewise, comparable pairs at 13 sites are plotted for OMPS-N20, which satisfied the minimum number of 90 pixels for OMPS-N20 and five or more matching monthly mean pairs conditions. Both OMPS-NPP/N20 have good correlation coefficients,  $R$ , of 0.83 and 0.88 with FTIR for all sites, respectively. However, OMPS-N20 has better statistics in terms of regression slopes, y-intercept, root mean square error (RMSE), NME, and normalized mean biases (NMBs),  $\frac{\sum(\text{OMPS} - \text{FTIR})}{\sum \text{FTIR}}$ , than OMPS-NPP. This suggests that OMPS-N20 can discern heterogeneous spatial patterns due to finer spatial pixel sizes than OMPS-NPP, as discussed in Section 3.2.

OMPS-NPP/N20 seem to have low biases following the linear relationship shown in Figure 2, but biases depend on sites and HCHO concentrations. Figure 3 shows OMPS-NPP/N20 biases with their uncertainties at each site. Bias and its uncertainty are defined following Vigouroux et al. (2020):

$$\text{Bias} = \text{median} \left( \frac{\text{OMPS}_i - \text{FTIR}_i}{\text{FTIR}_i} \right) \quad (2)$$

$$\text{MAD} = k \times \text{median} \left( \left| \left( \frac{\text{OMPS}_i - \text{FTIR}_i}{\text{FTIR}_i} \right) - \text{Bias} \right| \right) \quad (3)$$

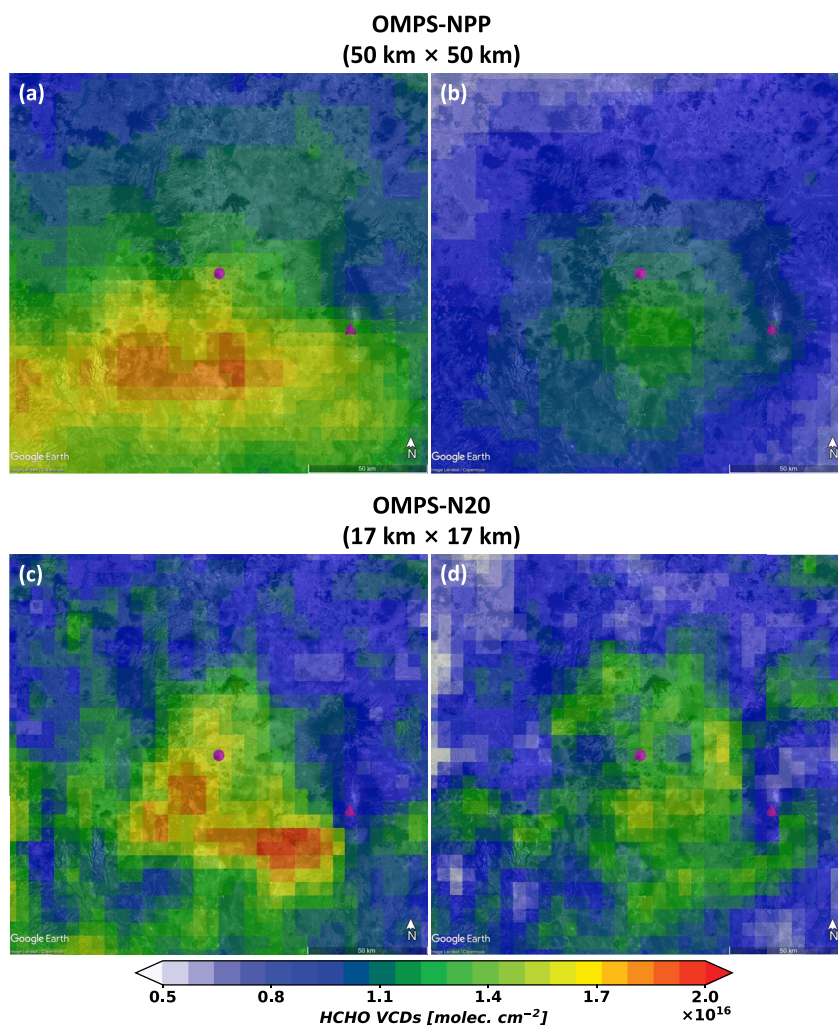
$$u_B = \frac{\text{MAD}}{\sqrt{n}} \quad (4)$$

$$U_B = 2 \times u_B \quad (5)$$

where  $\text{OMPS}_i$  and  $\text{FTIR}_i$  are comparable monthly mean pairs ( $i = 1, \dots, n$ ),  $n$  is the number of the pairs, MAD is the median absolute deviation converted to  $1\sigma$  standard deviation for normal distributions with a factor of  $k = 1/\Phi^{-1}(3/4) \approx 1.4826$  ( $\Phi^{-1}(x)$  is the inverse of the cumulative distribution function of normal distributions), and  $u_B$  and  $U_B$  are the standard uncertainty of bias and the expanded uncertainty of bias with a coverage factor of 2 having a level of confidence of  $\sim 95\%$ , respectively.

In Figure 3a, OMPS-NPP biases are within  $\pm 50\%$  at most sites except for three sites (Zugspitze, Altzomoni, and Porto Velho), and the bias at all sites is  $-0.9\% \pm 3\%$ . However, in most regions with relatively low HCHO VCDs ( $< 4.0 \times 10^{15}$  molecules  $\text{cm}^{-2}$ ), biases are positive ( $20\% \pm 6\%$ ) and decrease as HCHO VCDs increase. Some





**Figure 4.** Oversampled OMPS-NPP HCHO vertical column densities (VCDs) with a horizontal resolution of  $0.05^\circ$  in June–August (summer; a) and December–February (winter; b) for 2018–2020. Oversampled OMPS-N20 HCHO VCD in summer (c) and winter (d) in 2018–2020. Circle and triangle marks in magenta are Mexico City and Altzomoni sites, respectively.

sites such as Mauna Loa, Zugspitze, Izaña, Maïdo, and Altzomoni are located at high altitudes. At those sites, HCHO VCDs from satellites are higher than those from FTIR. While the FTIR measures the total column above site locations, total columns from satellites are derived over satellite footprints, and satellite pixels are sampled within a certain collocation distance (herein  $0.5^\circ$ ). Therefore, satellite observations can be affected by adjacent sources and larger backgrounds at lower altitudes, leading to higher HCHO VCDs from satellites at high-altitude sites compared to FTIR. In particular, the positive biases at Zugspitze are remarkable due to adjacent anthropogenic and biogenic sources. In Figure 4, OMPS-NPP HCHO VCDs at Altzomoni are higher than OMPS-N20 in summer because adjacent sources can increase retrieved HCHO values on the large pixel sizes of OMPS-NPP. Also, OMPS-NPP seasonal variation at Altzomoni in Figure 7 is similar to that at Mexico City, implying OMPS-NPP validation results could be affected by large spatial pixel size. This is discussed in more detail in Section 3.2.

On the other hand, at sites with relatively high HCHO VCDs ( $>4.0 \times 10^{15}$  molecules  $\text{cm}^{-2}$ ), HCHO VCDs from OMPS-NPP are lower than those from FTIR, with a bias of  $-15\% \pm 4\%$ . The negative bias is smaller than but generally in line with the previous validation results in Korea (Choi et al., 2022; Souri et al., 2020).

Figure 3b shows OMPS-N20 bias against FTIR observations with an overall small bias of  $4\% \pm 6\%$  at all sites. In the case of HCHO VCD  $<4.0 \times 10^{15}$  molecules  $\text{cm}^{-2}$ , OMPS-N20 shows a bias of  $32\% \pm 18\%$ , larger than OMPS-NPP despite the finer spatial pixel sizes for OMPS-N20. However, OMPS-N20 has smaller biases ( $0.5\% \pm 6\%$ ) in sites with HCHO VCDs  $>4.0 \times 10^{15}$  molecules  $\text{cm}^{-2}$  compared to OMPS-NPP, implying heterogeneous HCHO

distributions would be more discernible in OMPS-N20 and indicating the importance of satellite pixel sizes and signal-to-noise ratios.

At two South American sites (Paramaribo and Porto Velho), OMPS-NPP HCHO VCDs are higher than those from FTIR despite being sites with HCHO VCD  $> 4.0 \times 10^{15}$  molecules  $\text{cm}^{-2}$ . OMPS-NPP results might be higher than FTIR because adjacent biogenic sources and biomass burning can affect OMPS-NPP results with large pixels, but at Porto Velho, OMPS-N20 still shows high HCHO VCDs. Also, we find that cloud information has a significant impact on the results at these two sites. When we filter out OMPS-NPP pixels with cloud fraction  $> 0.1$  instead of 0.4, the bias at Porto Velho decreases from  $57\% \pm 24\%$  to  $-2\% \pm 63\%$ , although the expanded uncertainty of bias ( $U_B$ ) increases due to the small number of samples (from 17 to 9). At Paramaribo, the bias decreases from  $39\% \pm 81\%$  to  $14\% \pm 46\%$ .

We test the dependency of our results with respect to the cloud fraction filter threshold. The results using a cloud fraction of 0.1 are, for the most part, consistent with the results obtained with a 0.4 cloud fraction. However, the biases decrease at most sites, leading to an overall negative bias of OMPS products against FTIR (Figure S1 and Tables S1 and S2 in Supporting Information S1). Cloud effects on OMPS HCHO VCDs are more dominant in low HCHO conditions than in high HCHO conditions. Therefore, a careful selection of the cloud fraction filter threshold is required in low HCHO conditions such as rural areas and winter.

In addition, cloud fraction for OMPS-NPP/N20 is determined with the linear relationship between OMPS-NPP Raman cloud fraction and reflectivity from total ozone products (Nowlan et al., 2022). Therefore, aerosols from biomass burning might increase cloud fractions and affect AMF calculations, resulting in positive biases. It is important to investigate the details in further studies to improve consistent OMPS-NPP/N20 products, and cloud information should be updated for OMPS-NPP/N20.

We also compare daily average OMPS-NPP/N20 and FTIR observations. To have enough daily mean coincidences, we reduce the minimum required number of matching pixels from 10 to 5. The results of daily mean comparisons are similar to monthly mean results. There is a positive bias ( $11\% \pm 5\%$ ) in HCHO VCDs  $< 4.0 \times 10^{15}$  molecules  $\text{cm}^{-2}$  and a negative bias ( $-11\% \pm 3\%$ ) in HCHO VCDs  $> 4.0 \times 10^{15}$  molecules  $\text{cm}^{-2}$  (Figures S2a and S3a in Supporting Information S1). However, the correlation coefficient, RMSE, and NME are worse than those from monthly mean validation due to random noise (Figure S2a in Supporting Information S1).

For OMPS-N20, which has a higher noise level than OMPS-NPP, it is difficult to achieve similar reductions of noise level in the daily means under the current conditions (spatial sampling grid of  $0.5^\circ$  and a temporal window of  $\pm 3$  hr); so, to have enough samples, we reduce the minimum number of matching pixels from 90 to 20. As OMPS-NPP for daily mean comparison, OMPS-N20 has a worse correlation coefficient and higher RMSE and NME than those from monthly mean comparisons (Figure S2b in Supporting Information S1). Bias of daily means between OMPS-N20 and FTIR is 2.4% in the low HCHO VCD condition ( $< 4.0 \times 10^{15}$  molecules  $\text{cm}^{-2}$ ), which is smaller than that of monthly mean comparisons, but its uncertainty is 22% due to the large variability (Figure S3b in Supporting Information S1). In HCHO VCDs  $> 4.0 \times 10^{15}$  molecules  $\text{cm}^{-2}$ , the bias of  $1.5\% \pm 6\%$  is similar to that in the monthly mean comparisons ( $0.5\% \pm 6\%$ ). Therefore, OMPS-NPP/N20 daily means show similar biases compared to FTIR observations, but it is noted that daily means can vary if satellite pixels are not enough to reduce noise.

Tables 3 and 4 summarize statistics of OMPS-NPP/N20 validation results compared to FTIR at each site. At sites with relatively high HCHO VCDs ( $> 4.0 \times 10^{15}$  molecules  $\text{cm}^{-2}$ ), OMPS-NPP has very good agreement with FTIR except for three sites (Saint-Denis, Palau, and Rikubetsu), which can be classified as rural sites. Most sites show good correlation coefficients ranging from 0.75 to 0.92, but the correlation between OMPS-NPP and FTIR at Paramaribo, Boulder, and Mexico City is relatively low. The averaged FTIR HCHO VCD at Paramaribo is  $6.5 \times 10^{15}$  molecules  $\text{cm}^{-2}$  from original FTIR data shown in Figure 3 and Table 3, but  $3.7 \times 10^{15}$  molecules  $\text{cm}^{-2}$  after a priori profile corrections and AK smoothing. Also, the number of pairs  $< 4.0 \times 10^{15}$  molecules  $\text{cm}^{-2}$  accounts for 80% of all pairs at Paramaribo, leading to a lower correlation than at other sites. The small number of comparable pairs at Boulder leads to a relatively low correlation coefficient. The Mexico City site has high heterogeneity, with HCHO concentrations being affected by biogenic sources near Mexico City as well as anthropogenic activities. This is discussed further in Section 3.2.

In comparison with OMPS-NPP, OMPS-N20 with its finer spatial pixel size shows better correlation coefficients at all sites, except for Paris, with HCHO VCDs  $> 4.0 \times 10^{15}$  molecules  $\text{cm}^{-2}$ , although data have been collected

**Table 3**  
Statistics of OMPS-NPP Validation Compared With FTIR, Sorted by Mean HCHO VCDs From FTIR

Station	Mean VCD (molec. cm <sup>-2</sup> )	Bias ± U <sub>B</sub> (%)	R	Slope (u <sub>a</sub> )	Offset (u <sub>b</sub> ; molec. cm <sup>-2</sup> )	N
Mauna Loa	1.2 × 10 <sup>15</sup>	36 ± 22	0.14	0.2 (0.2)	1.2 (0.2) × 10 <sup>15</sup>	38
Zugspitze	1.7 × 10 <sup>15</sup>	88 ± 28	0.60	1.5 (0.3)	0.7 (0.4) × 10 <sup>15</sup>	26
Izaña	1.9 × 10 <sup>15</sup>	21 ± 8	0.71	1.3 (0.1)	−0.2 (0.1) × 10 <sup>15</sup>	88
Maïdo	2.2 × 10 <sup>15</sup>	2 ± 7	0.58	1.0 (0.1)	−0.1 (0.2) × 10 <sup>15</sup>	67
Altzomoni	2.6 × 10 <sup>15</sup>	52 ± 19	0.25	0.5 (0.1)	2.1 (0.3) × 10 <sup>15</sup>	45
Kiruna	3.0 × 10 <sup>15</sup>	20 ± 38	0.27	1.0 (0.3)	0.1 (0.6) × 10 <sup>15</sup>	24
Lauder	3.4 × 10 <sup>15</sup>	−4 ± 14	0.15	0.6 (0.2)	1.2 (0.5) × 10 <sup>15</sup>	42
Sodankyla	3.5 × 10 <sup>15</sup>	28 ± 20	0.32	0.5 (0.1)	1.8 (0.3) × 10 <sup>15</sup>	32
Saint-Denis	4.7 × 10 <sup>15</sup>	−20 ± 18	0.47	0.02 (0.3)	2.4 (1.1) × 10 <sup>15</sup>	17
Palau	4.7 × 10 <sup>15</sup>	−23 ± 42	−0.30	−0.2 (0.3)	4.2 (1.0) × 10 <sup>15</sup>	7
Rikubetsu	5.0 × 10 <sup>15</sup>	−16 ± 54	−0.02	−0.4 (0.2)	5.0 (0.6) × 10 <sup>15</sup>	11
Paramaribo	6.5 × 10 <sup>15</sup>	39 ± 81	0.62	1.0 (0.2)	1.2 (0.7) × 10 <sup>15</sup>	16
St. Petersburg	7.2 × 10 <sup>15</sup>	−6 ± 12	0.77	0.8 (0.1)	0.5 (0.4) × 10 <sup>15</sup>	43
Bremen	8.0 × 10 <sup>15</sup>	8 ± 15	0.82	1.0 (0.1)	0.4 (0.4) × 10 <sup>15</sup>	35
Tsukuba	8.1 × 10 <sup>15</sup>	−27 ± 13	0.75	1.7 (0.1)	−4.8 (0.5) × 10 <sup>15</sup>	58
Wollongong	8.4 × 10 <sup>15</sup>	−33 ± 6	0.92	0.7 (0.03)	−0.2 (0.3) × 10 <sup>15</sup>	65
Paris	8.7 × 10 <sup>15</sup>	−11 ± 10	0.75	0.8 (0.1)	0.5 (0.4) × 10 <sup>15</sup>	49
Karlsruhe	8.7 × 10 <sup>15</sup>	−5 ± 15	0.88	1.3 (0.1)	−2.7 (0.8) × 10 <sup>15</sup>	17
Toronto	9.9 × 10 <sup>15</sup>	−6 ± 10	0.85	1.6 (0.1)	−4.7 (0.6) × 10 <sup>15</sup>	60
Boulder	9.9 × 10 <sup>15</sup>	20 ± 16	0.40	1.3 (0.3)	0.3 (2.1) × 10 <sup>15</sup>	10
Xianghe	1.5 × 10 <sup>16</sup>	−18 ± 9	0.86	1.1 (0.1)	−3.1 (0.9) × 10 <sup>15</sup>	21
Porto Velho	1.8 × 10 <sup>16</sup>	57 ± 24	0.75	1.4 (0.1)	0.7 (1.2) × 10 <sup>15</sup>	17
Mexico City	2.3 × 10 <sup>16</sup>	−29 ± 9	0.45	0.3 (0.1)	6.5 (1.1) × 10 <sup>15</sup>	51
All sites	7.2 × 10 <sup>15</sup>	−0.9 ± 3	0.83	0.8 (0.01)	0.6 (0.03) × 10 <sup>15</sup>	839
HCHO VCDs <4.0 × 10 <sup>15</sup>	2.4 × 10 <sup>15</sup>	20 ± 6	0.43	0.9 (0.04)	0.4 (0.1) × 10 <sup>15</sup>	362
HCHO VCDs >4.0 × 10 <sup>15</sup>	9.8 × 10 <sup>15</sup>	−15 ± 4	0.78	0.9 (0.01)	0.1 (0.1) × 10 <sup>15</sup>	477

Note. U<sub>B</sub> is the expanded uncertainty of bias, R is the correlation coefficient, u<sub>a</sub> and u<sub>b</sub> are the standard uncertainties of slope and offset, and N is the number of comparable monthly average pairs between OMPS-NPP and FTIR.

only since 2018 and therefore the number of available coincident observations is small compared with those available from OMPS-NPP. The bias of 0.5% ± 6% for OMPS-N20 is smaller than the −15% ± 4% determined for OMPS-NPP. Improvement of both the correlation coefficient and bias is remarkable at Mexico City, which has various source regions surrounded by complex topography. This implies that OMPS-N20, with finer pixel sizes, can discern heterogeneous HCHO plumes and minimize the effects of complex terrain heights on HCHO VCDs, leading to better agreements with FTIR than OMPS-NPP.

### 3.2. Importance of Spatial Pixel Sizes

OMPS-N20 has ~9 times finer spatial sampling than OMPS-NPP as a result of a trade-off with low signal-to-noise. OMPS-N20 shows noisier pixel-to-pixel HCHO VCDs in one orbit compared to OMPS-NPP, but as we discussed in Section 3.1, OMPS-N20 monthly mean results are superior to those of OMPS-NPP, distinguishing complex sources and providing better agreement with FTIR observations. Here, we discuss the importance of spatial pixel sizes from the two very similar instruments.

Figure 4 shows oversampled OMPS-NPP/N20 HCHO VCDs in June–August (summer) and December–February (winter) for 3 years (2018–2020) over Mexico City and surrounding areas. In summer, HCHO VCDs are high

**Table 4**  
Same as Table 3 But for OMPS-N20

Station	Mean VCDs (molec. cm <sup>-2</sup> )	Bias ± U <sub>B</sub> (%)	R	Slope (u <sub>a</sub> )	Offset (u <sub>b</sub> ; molec. cm <sup>-2</sup> )	N
Izaña	1.9 × 10 <sup>15</sup>	32 ± 23	0.60	0.8 (0.3)	1.0 (0.6) × 10 <sup>15</sup>	12
Maïdo	2.2 × 10 <sup>15</sup>	25 ± 21	0.51	0.5 (0.2)	1.2 (0.3) × 10 <sup>15</sup>	17
Kiruna	3.2 × 10 <sup>15</sup>	38 ± 65	0.29	0.3 (1.0)	2.6 (2.0) × 10 <sup>15</sup>	5
Lauder	3.5 × 10 <sup>15</sup>	80 ± 25	-0.49	-0.3 (0.6)	5.1 (1.6) × 10 <sup>15</sup>	6
Sodankyla	4.4 × 10 <sup>15</sup>	23 ± 17	0.68	0.9 (0.4)	1.1 (1.3) × 10 <sup>15</sup>	7
St. Petersburg	7.1 × 10 <sup>15</sup>	2 ± 20	0.86	0.7 (0.2)	2.2 (1.2) × 10 <sup>15</sup>	9
Karlsruhe	8.7 × 10 <sup>15</sup>	7 ± 12	0.91	1.1 (0.1)	0.03 (0.7) × 10 <sup>15</sup>	17
Paris	9.4 × 10 <sup>15</sup>	-8 ± 21	0.69	0.9 (0.1)	0.5 (1.2) × 10 <sup>15</sup>	10
Toronto	9.8 × 10 <sup>15</sup>	0.4 ± 9	0.89	1.2 (0.1)	-1.2 (0.9) × 10 <sup>15</sup>	14
Wollongong	1.1 × 10 <sup>16</sup>	-26 ± 8	0.94	0.6 (0.05)	1.2 (0.5) × 10 <sup>15</sup>	17
Xianghe	1.6 × 10 <sup>16</sup>	5 ± 10	0.89	0.8 (0.1)	3.0 (0.8) × 10 <sup>15</sup>	17
Mexico City	2.0 × 10 <sup>16</sup>	0.3 ± 8	0.71	0.7 (0.2)	4.3 (3.9) × 10 <sup>15</sup>	9
Porto Velho	2.3 × 10 <sup>16</sup>	63 ± 60	0.83	1.4 (0.1)	5.0 (1.7) × 10 <sup>15</sup>	5
All sites	9.2 × 10 <sup>15</sup>	4 ± 6	0.88	0.9 (0.02)	0.7 (0.1) × 10 <sup>15</sup>	145
HCHO VCDs <4.0 × 10 <sup>15</sup>	2.7 × 10 <sup>15</sup>	32 ± 18	0.47	0.6 (0.1)	1.2 (0.3) × 10 <sup>15</sup>	40
HCHO VCDs >4.0 × 10 <sup>15</sup>	1.2 × 10 <sup>16</sup>	0.5 ± 6	0.84	0.9 (0.02)	0.9 (0.2) × 10 <sup>15</sup>	105

in the south of Mexico City resulting from biogenic activities and predominant north and northeastern winds. HCHO VCD enhancement in Mexico City resulting from anthropogenic emissions is not discernible by OMPS-NPP and is diluted by low HCHO VCDs in the north of Mexico City. Also, areas with relatively low HCHO are affected by adjacent HCHO sources due to large pixel sizes of OMPS-NPP, resulting in positive biases at Altzomoni site in comparison with FTIR.

Due to finer pixel sizes, however, OMPS-N20 can discern anthropogenic HCHO plumes over Mexico City and its surroundings, and HCHO VCDs are more concentrated in source regions. Also, OMPS-N20 HCHO VCDs at Altzomoni are less contaminated by adjacent sources than those from OMPS-NPP. The enhanced capabilities of OMPS-N20 are more clearly seen during winter with smaller widespread biogenic emissions. OMPS-N20 shows HCHO enhancements in Mexico City and adjacent source regions due to agricultural burning while OMPS-NPP cannot capture HCHO source regions because of diluted HCHO VCDs.

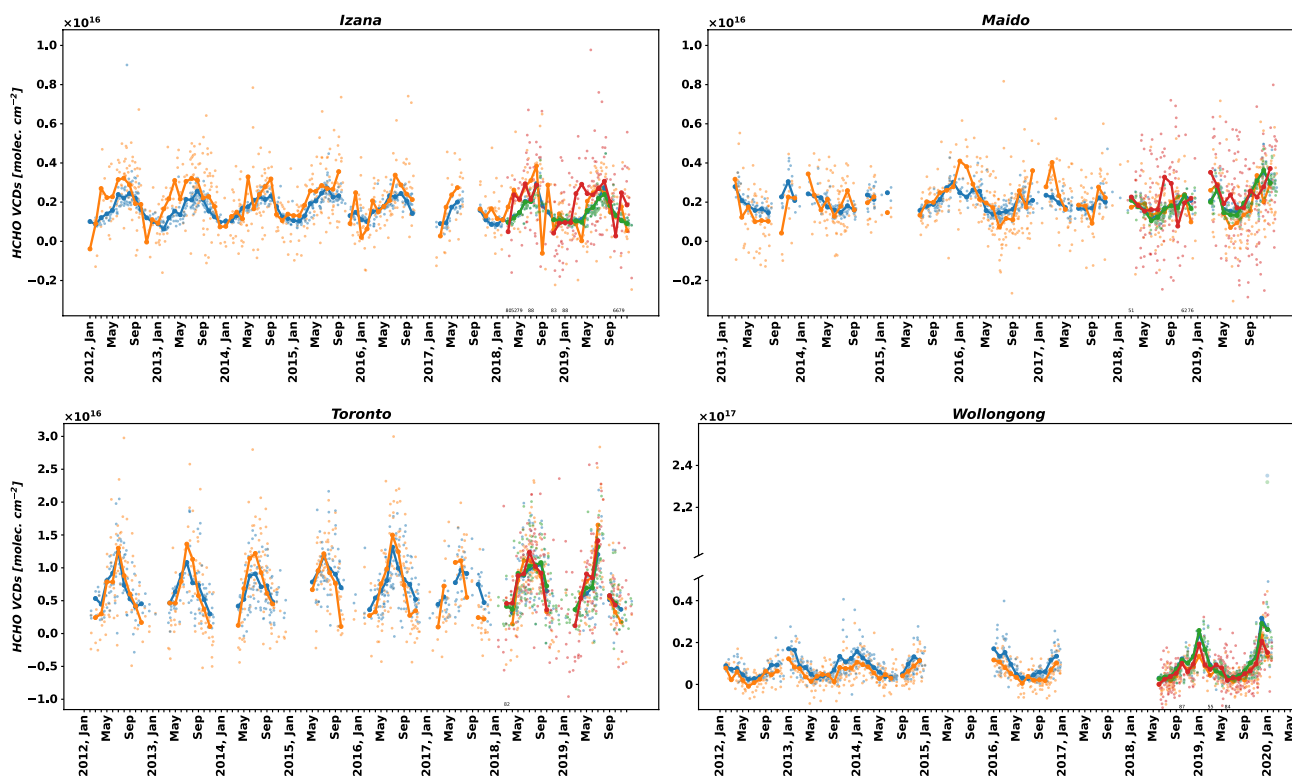
Therefore, OMPS-N20 has a smaller bias and better agreement with FTIR compared to OMPS-NPP as shown in Section 3.1. It reflects that the OMPS-N20 level 2 products with small pixel sizes, despite low signal-to-noise ratio, have the advantage of discerning complex and inhomogeneous plumes using temporal averages if compared with correlative OMPS-NPP observations. If target species can be retrieved with a relatively low signal-to-noise ratio and a signal-to-noise ratio is not required to obtain precise information on each pixel, the use of the native spatial pixel size of the instruments would be helpful to detect and monitor emissions of pollutants on small scales.

### 3.3. Monthly and Seasonal Variability of OMPS-NPP/N20 HCHO VCDs

Figure 5 shows FTIR and OMPS-NPP monthly variations at four sites, where observations were available over 6 years, to evaluate the long-term variability and stability of the satellite retrievals. These four sites have good correlation coefficients from 0.58 to 0.92. At the Izaña and Maïdo sites, located in clean areas, correlation coefficients are smaller than those for the polluted sites of Wollongong and Toronto. Despite low levels of HCHO at the clean sites, OMPS-NPP at these sites shows consistent monthly variations with FTIR.

OMPS-NPP at the two polluted sites (Wollongong and Toronto) also shows consistent monthly variations with FTIR. At Wollongong, HCHO VCDs from both OMPS-NPP and FTIR were enhanced in December 2019 and January 2020 due to massive Australian bushfires. HCHO VCD from OMPS-NPP is  $2.3 \times 10^{16}$  molecules cm<sup>-2</sup> in December 2019, which is 2.5 times larger than an annual mean in December ( $9.5 \times 10^{15}$  molecules cm<sup>-2</sup>). However, HCHO VCDs from OMPS-NPP are -26% lower than FTIR observations, and OMPS-N20 also has





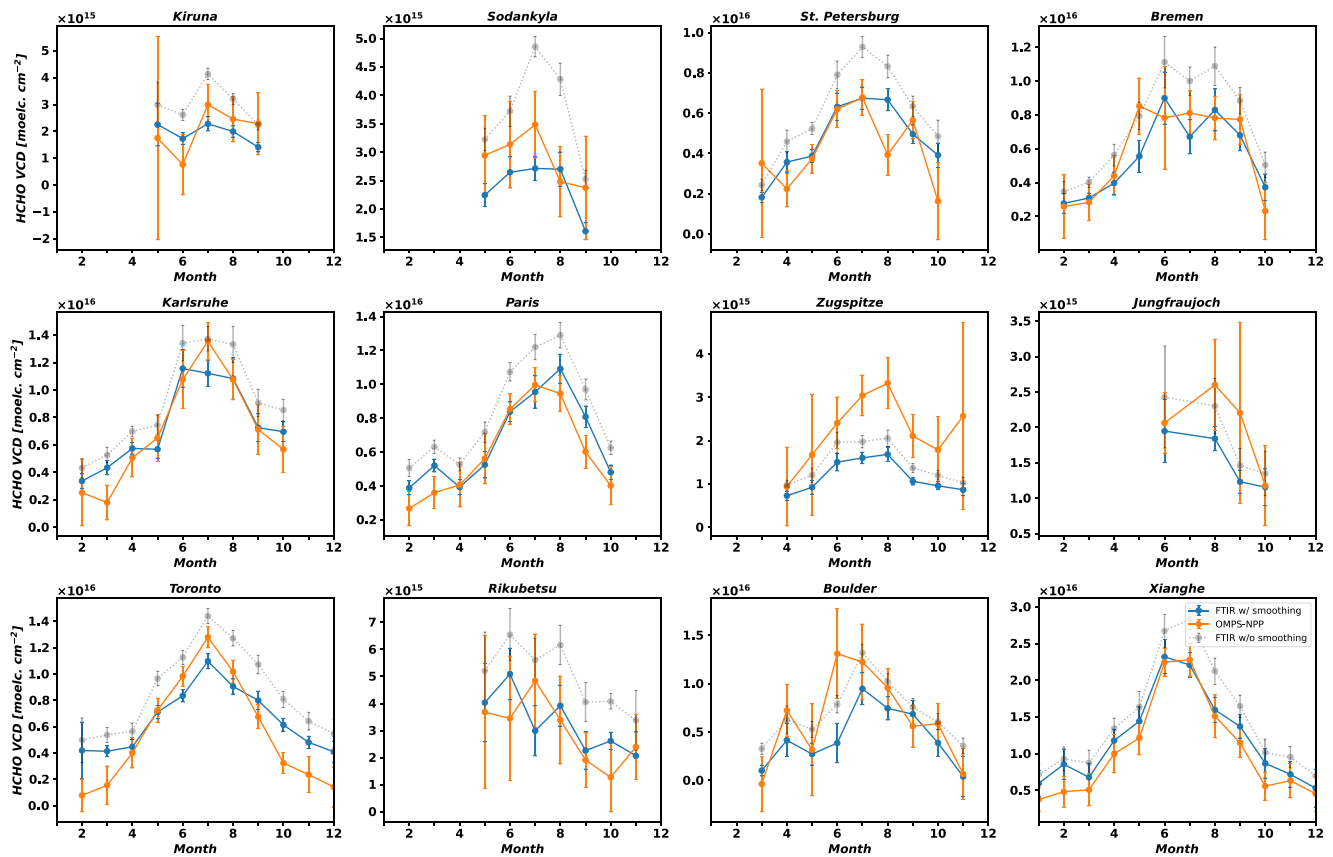
**Figure 5.** Collocated monthly mean time series (solid lines) of OMPS-NPP (orange), OMPS-N20 (red), and Fourier-Transform Infrared (FTIR) HCHO vertical column densities (VCDs). The two FTIR lines (blue and green) correspond with OMPS-NPP/N20, respectively. Small dots indicate daily mean HCHO VCDs from each instrument.

−29% biases compared to FTIR observations in December 2019. In addition, HCHO VCD from FTIR is enhanced by  $2.4 \times 10^{17}$  molecules  $\text{cm}^{-2}$  on 31 December 2019, while HCHO VCD from OMPS-NPP is  $4.4 \times 10^{16}$  molecules  $\text{cm}^{-2}$ . Therefore, OMPS observations over episodic biomass burnings need to be used carefully since HCHO profiles over biomass burning areas are most likely different from the climatological a priori profile used in the OMPS HCHO algorithm, and biomass burning aerosols could affect the accuracy of the scattering weights.

OMPS-N20 results also show consistent monthly variations with OMPS-NPP and FTIR observations. At the two polluted sites of Toronto and Wollongong, OMPS-N20 shows correlations of 0.89 and 0.94. As expected, smaller correlations of 0.60 and 0.51 are found over the Izaña and Maïdo sites. As discussed above, OMPS-N20 has lower precision than OMPS-NPP due to smaller pixel sizes, and retrievals in clean regions are more sensitive to random noise in the measurements. This is shown by the scatter of daily OMPS-N20 observations in comparison with those from OMPS-NPP and FTIR. At Izaña, for example, the precision of daily means from OMPS-NPP is  $1.7 \times 10^{15}$  molecules  $\text{cm}^{-2}$  while the one from OMPS-N20 is  $2.1 \times 10^{15}$  molecules  $\text{cm}^{-2}$ .

Figures 6 and 7 shows HCHO VCD overall seasonal variability from FTIR and OMPS-NPP by site for 2012–2022. The Jungfraujoch site is included in this analysis as enough pixels can be gathered from multiple years to examine seasonal variability. Panels are sorted by decreasing latitude, from North to South (see Table 2 for their precise coordinates). Seasonal variability in OMPS-NPP HCHO has good agreement with that observed by the FTIR. At most sites, HCHO VCDs are high in the summer of the Northern Hemisphere (June–August) and Southern Hemisphere (December–February) due to increases in both photochemistry and biogenic sources.

HCHO VCDs over some clean regions such as Mauna Loa and Palau do not have significant seasonal variability. However, at sites such as Zugspitze, Jungfraujoch, and Maïdo on the island of Réunion, which are located at high altitude in relatively clean atmospheres, distinct seasonal variability is shown in the summer season. Franco et al. (2016) showed the seasonal variability of HCHO total columns above Jungfraujoch could be due to the methane oxidation from the model sensitivity test. Likewise, the seasonal variability at Zugspitze, close to Jungfraujoch, might also result from methane oxidation.



**Figure 6.** HCHO vertical column density (VCD) seasonal variations of Fourier-Transform Infrared (FTIR) and OMPS-NPP at each FTIR site. Blue and orange solid lines with circle dots denote FTIR with a priori profile correction and averaging kernel (AK) smoothing and OMPS-NPP HCHO VCDs, respectively, and gray dotted lines with circle dots denote FTIR HCHO VCDs without the correction and smoothing. Error bars denote the expanded uncertainties with a coverage factor of 2 ( $\pm 2 \times \sigma_w$ ).

Some sites (Mexico City, Altzomoni, Paramaribo, and Porto Velho) are affected by anthropogenic and biogenic HCHO precursors and biomass burning and show different seasonal variability. At two sites in South America (Paramaribo and Porto Velho), for example, FTIR and OMPS-NPP HCHO VCDs are enhanced in the dry season (July–November) due to biogenic sources and biomass burning (Gonzalez-Alonso et al., 2019; Malhi et al., 2008). The Mexico City site has peaks of HCHO VCDs in May at the beginning of the rainy season, and biogenic sources as well as anthropogenic sources can affect HCHO VCDs (Amador-Muñoz et al., 2011; Rivera Cárdenas et al., 2021).

In Figures 8 and 9, interannual averages of OMPS-N20 at each month for 2018–2020 also have good agreement with FTIR observations but relatively large uncertainties because the ideal number of sample pairs for OMPS-N20 (90 pixels) is not satisfied. For the OMPS-N20 analysis, the Saint-Denis site on the island of Réunion is excluded because FTIR observations ended in June 2015 before OMPS-N20 was launched. OMPS-N20 observations show the typical seasonal variability, with high HCHO VCDs in summer.

At some sites, different seasonal variability is shown between OMPS-NPP/N20 and FTIR. Partially this is discussed in Sections 3.1 and 3.2. At elevated sites including Mauna Loa, Zugspitze, Izaña, Mäido, and Altzomoni, given the satellite footprints, observations are affected by nearby sources situated below the FTIR instruments, resulting in higher HCHO VCDs and different seasonal patterns. Additionally, the presence of clouds, aerosols, and a priori profiles can also contribute to varying seasonal patterns in HCHO VCDs between OMPS-NPP/N20 and FTIR measurements.

#### 4. Uncertainty of OMPS-NPP/N20 HCHO Products

Satellite observations need to be considered with their associated uncertainties arising from random and systematic effects. For example, uncertainties are important to characterize a priori covariance matrices in inverse modeling studies to estimate emissions from the observations. Most satellite observations are used by averaging

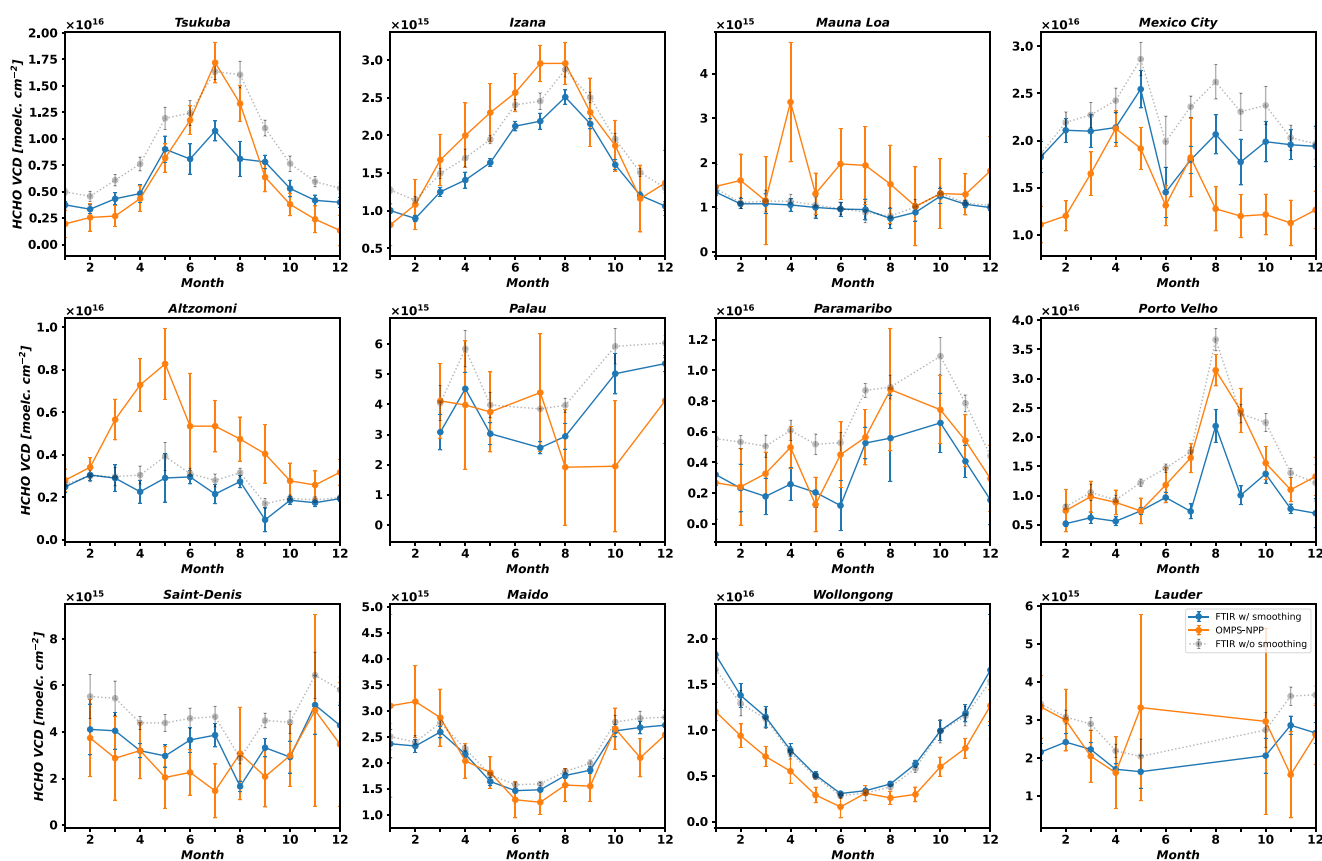


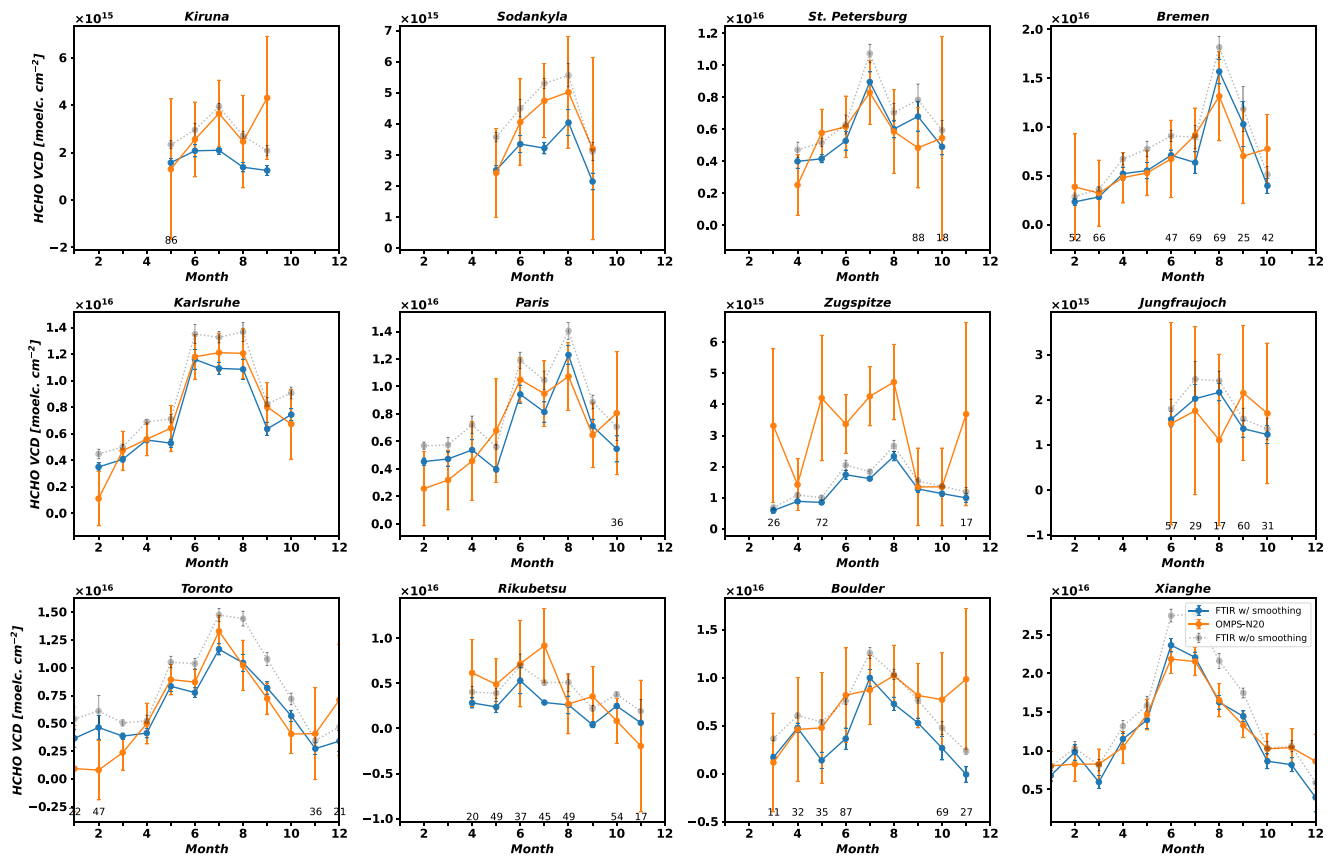
Figure 7. Same as Figure 6, but for the next 12 sites.

pixels to make satellite observations coincident with a horizontal grid of a model and to reduce random noises in weakly absorbing trace gases such as HCHO. In these cases, uncertainties on each pixel from random sources can be combined through uncertainty propagation and with arithmetic means for uncertainty arising from systematic effects (Souri et al., 2021). However, it is difficult to estimate the uncertainty of all parameters and correlations between parameters in retrievals.

Instead, ground-based and in situ aircraft observations with higher accuracy than satellite observations have been used to estimate the uncertainty of remote sensing observations from satellite and aircraft platforms (De Smedt et al., 2021; Nowlan et al., 2018; Vigouroux et al., 2020; Zhu et al., 2020). Vigouroux et al. (2020) quantitatively evaluated the uncertainty of TROPOMI HCHO products with biases and MAD from FTIR.

We provide here information about the uncertainty of OMPS-NPP/N20 HCHO monthly mean products ( $u_{\text{OMPS}}$ ) using the bias and MAD when compared to FTIR observations as a reference quantity, while acknowledging that FTIR observations are not true values. The uncertainty of the bias in Equation 4 could be considered as the uncertainty of OMPS-NPP/N20 because the variability of bias can be caused by retrieval errors, input data such as surface reflectance, a priori profile, and cloud information, natural variability, and exceptional events like biomass burning. However, FTIR is imperfect and is not a true value, and the bias does not perfectly follow the Gaussian distribution. Instead, a symmetric triangular probability function with the range of  $\pm 2 \times \text{MAD}$  is assumed, and the systematic uncertainty is calculated as a standard deviation of the symmetric triangular probability function ( $\frac{2 \times \text{MAD}}{\sqrt{6}}$ ). Detail sources of uncertainty are described in Nowlan et al. (2022).

OMPS-NPP HCHO monthly means at all sites have a bias of  $-0.9\% \pm 3\%$  compared to FTIR observations and an uncertainty of  $1.5 \times 10^{15}$  molecules  $\text{cm}^{-2}$ . The total uncertainty of OMPS-N20 products with the bias of  $4\% \pm 6\%$  is  $1.2 \times 10^{15}$  molecules  $\text{cm}^{-2}$ , similar to OMPS-NPP uncertainty. In clean sites with HCHO VCDs  $< 4.0 \times 10^{15}$  molecules  $\text{cm}^{-2}$ , OMPS-NPP/N20 have biases of  $20\% \pm 6\%$  and  $32\% \pm 18\%$ , respectively, with similar uncertainties of  $0.7 \times 10^{15}$  and  $0.8 \times 10^{15}$  molecules  $\text{cm}^{-2}$ . In the case of HCHO VCDs  $> 4.0 \times 10^{15}$  mole-



**Figure 8.** HCHO vertical column density (VCD) seasonal variations of Fourier-Transform Infrared (FTIR) and OMPS-N20 at each FTIR site. Blue and orange solid lines with circle dots denote FTIR with a priori profile correction and averaging kernel (AK) smoothing and OMPS-N20 HCHO VCDs, respectively, and gray dotted lines with circle dots denote FTIR HCHO VCDs without the correction and smoothing. Error bars denote the expanded uncertainties with a coverage factor of 2 ( $\pm 2 \times \sigma_w$ ). The number of matches is provided for cases with less than 90 successful matchings.

cules  $\text{cm}^{-2}$ , the uncertainty of OMPS-N20 is  $1.7 \times 10^{15}$  molecules  $\text{cm}^{-2}$ , similar to the total uncertainty of  $2.3 \times 10^{15}$  molecules  $\text{cm}^{-2}$  for OMPS-NPP, but OMPS-N20 products are in better agreements with FTIR, showing a smaller bias of  $0.5\% \pm 6\%$  compared with  $-15\% \pm 4\%$  for OMPS-NPP.

The known systematic error (bias) can be corrected, and biases can be classified as proportional and constant biases (Vigouroux et al., 2020), corresponding to the slope ( $a$ ) and  $y$ -intercept ( $b$ ) in the linear least square method. The bias correction is conducted only at sites with high HCHO VCDs ( $>4.0 \times 10^{15}$  molecules  $\text{cm}^{-2}$ ) because most sites with HCHO VCDs  $>4.0 \times 10^{15}$  molecules  $\text{cm}^{-2}$  have high correlation coefficients. Corrected HCHO VCDs and their uncertainties are estimated as follows:

$$y_c = \frac{(y - b)}{a} \quad (6)$$

$$u_c^2 = \frac{(y - b)^2}{a^4} u_a^2 + \frac{1}{a^2} (u_y^2 + u_b^2) \quad (7)$$

where  $y$  and  $y_c$  are the satellite observations and the corrected ones, respectively, and  $u_c$ ,  $u_a$ , and  $u_b$  are the total uncertainty of the corrected observations, slope, and  $y$ -intercept, respectively.

Before the correction, the average HCHO VCD from OMPS-NPP is  $7.3 \times 10^{15}$  molecules  $\text{cm}^{-2}$ , and the relative uncertainty (the uncertainty), which is the ratio of the uncertainty to HCHO VCD, is 31% ( $2.3 \times 10^{15}$  molecules  $\text{cm}^{-2}$ ). As shown in Table 3, the bias of  $-15\% \pm 4\%$  represents the constant and proportional biases (their uncertainty) of  $0.1$  ( $0.1 \times 10^{15}$  molecules  $\text{cm}^{-2}$ ) and  $0.9$  (0.01), respectively. After the correction using Equation 6, the averaged HCHO VCD and uncertainty from OMPS-NPP increase to  $8.3 \times 10^{15}$  and  $2.6 \times 10^{15}$  molecules  $\text{cm}^{-2}$ ,



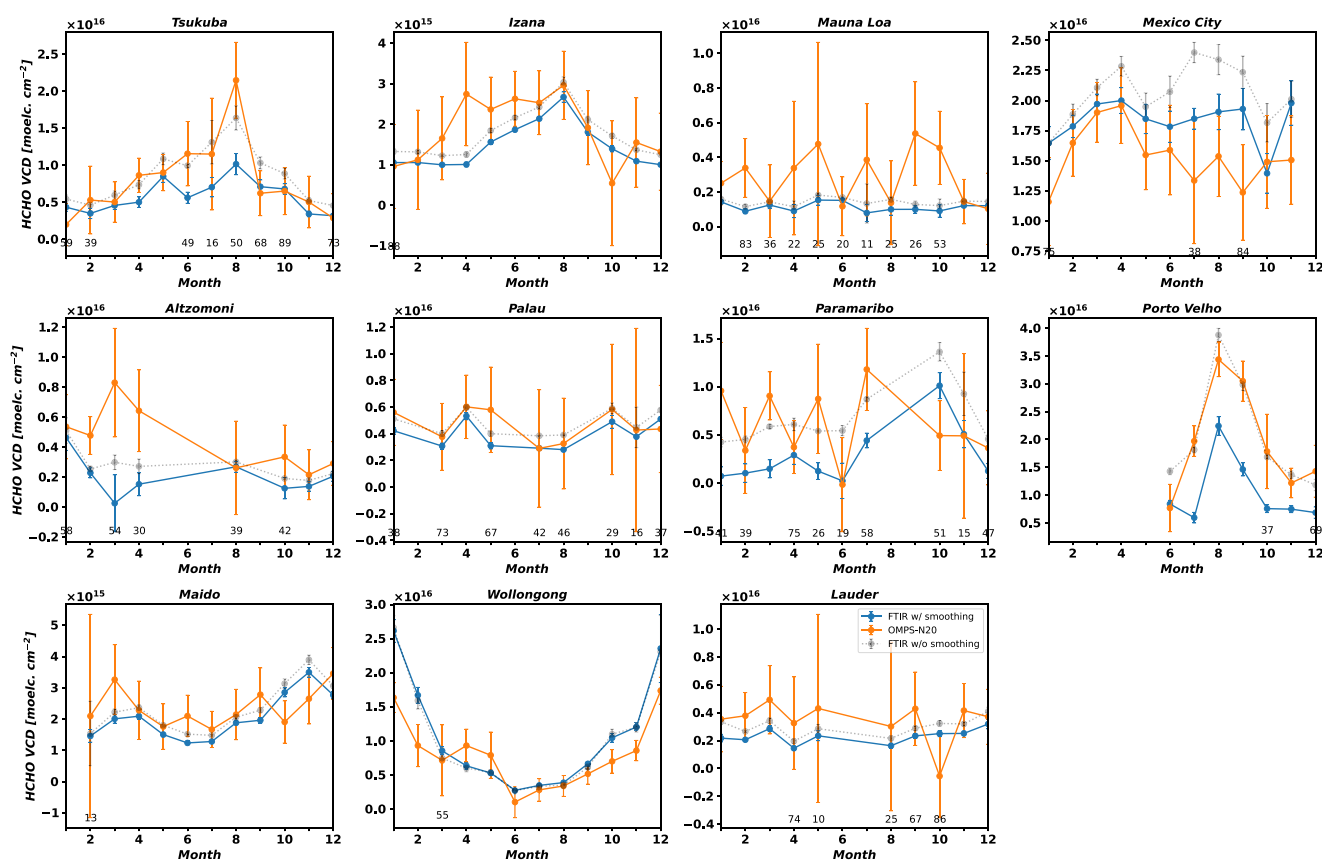


Figure 9. Same as Figure 8, but for the next 11 sites.

respectively, but a relative total uncertainty of 31% does not change compared to that before the bias correction. In OMPS-N20, the bias is small in high VCDs; therefore, the bias correction has the effect of increasing the uncertainty (the relative uncertainty) from  $1.7 \times 10^{15}$  molecules  $\text{cm}^{-2}$  (18%) to  $2.0 \times 10^{15}$  molecules  $\text{cm}^{-2}$  (20%). Table 5 summarizes the uncertainties of OMPS-NPP/N20 in different HCHO VCD conditions. However, please note that the uncertainty is estimated for the monthly mean and horizontal resolution of  $0.5^\circ$ . Also, the uncertainty and bias could change depending on the site, so great care should be considered in applying the bias correction and estimated uncertainties we present here.

### 5. Conclusions

OMPS-NPP/N20 HCHO VCDs for 2012–2020 and 2018–2020 are validated with FTIR ground-based observations at 24 sites. For temporally and spatially collocated pairs, FTIR observations within  $\pm 3$  hr are sampled, and OMPS-NPP/N20 pixels are collected in a grid cell of  $0.5^\circ$  with the center positioned at each site location. We consider a priori profile correction and AK smoothing to minimize the effects of a priori profiles and AK on retrieved HCHO VCDs between OMPS-NPP/N20 and FTIR.

Monthly mean HCHO VCDs from OMPS-NPP/N20 show a good agreement with FTIR observations; OMPS-N20 with finer ground pixel sizes shows a better correlation coefficient of 0.88 than that of 0.83 from OMPS-NPP. However, OMPS-NPP/N20 show biases that depend on site and the absolute value of HCHO VCDs when compared to FTIR observations. When considering all sites, the overall bias of OMPS-NPP (N20) is  $-0.9 (4) \pm 3 (6)\%$ . In the case of HCHO VCD  $> 4.0 \times 10^{15}$  molecules  $\text{cm}^{-2}$ , OMPS-NPP (N20) HCHO VCDs have low biases of  $-15 (0.5) \pm 4 (6)\%$ , while high biases of  $20 (32) \pm 6 (18)\%$  occur at cleaner sites with HCHO VCDs  $< 4.0 \times 10^{15}$  molecules  $\text{cm}^{-2}$ .

At sites with HCHO VCD  $> 4.0 \times 10^{15}$  molecules  $\text{cm}^{-2}$ , OMPS-NPP/N20 have better correlation coefficients ranging from 0.75 to 0.92 (except for Paramaribo, Boulder, and Mexico City) than at sites with low HCHO VCDs ( $< 4.0 \times 10^{15}$  molecules  $\text{cm}^{-2}$ ); OMPS-N20 with finer pixel sizes shows improvement of correlation coefficients

**Table 5**  
The Uncertainty Budget of OMPS-NPP for 2012–2020 and OMPS-N20 for 2018–2020

		OMPS HCHO VCD (molec. cm <sup>-2</sup> )	Bias ± $U_B$ (%)	$u_{OMPS}$ (molec. cm <sup>-2</sup> )	$\frac{u_{OMPS}}{HCHO\ VCD} \times 100$ (%)
All sites	NPP	$5.2 \times 10^{15}$	$-0.9 \pm 3$	$1.5 \times 10^{15}$	28
	N20	$7.7 \times 10^{15}$	$4 \pm 6$	$1.2 \times 10^{15}$	16
HCHO VCDs < $4.0 \times 10^{15}$ molec. cm <sup>-2</sup>	NPP	$2.3 \times 10^{15}$	$20 \pm 6$	$0.7 \times 10^{15}$	32
	N20	$2.7 \times 10^{15}$	$32 \pm 18$	$0.8 \times 10^{15}$	30
HCHO VCDs > $4.0 \times 10^{15}$ molec. cm <sup>-2</sup>	NPP	$7.3 \times 10^{15}$	$-15 \pm 4$	$2.3 \times 10^{15}$	31
	N20	$9.7 \times 10^{15}$	$0.5 \pm 6$	$1.7 \times 10^{15}$	18
Correction HCHO VCDs > $4.0 \times 10^{15}$ molec. cm <sup>-2</sup>	NPP	$8.3 \times 10^{15}$	$-3 \pm 4$	$2.6 \times 10^{15}$	31
	N20	$9.7 \times 10^{15}$	$-0.6 \pm 6$	$2.0 \times 10^{15}$	20

Note. Sites used to estimate the uncertainty are based on Tables 3 and 4.

compared to OMPS-NPP. This implies that OMPS-NPP/N20 can measure HCHO VCDs with better accuracy in the case of HCHO VCD >  $4.0 \times 10^{15}$  molecules cm<sup>-2</sup> and that smaller pixel sizes are important to discern heterogeneous spatial patterns in source regions.

OMPS-NPP/N20 HCHO retrievals at most sites show similar seasonal variability with high and low HCHO VCDs in summer and winter, respectively, due to variabilities in photochemical and biogenic activities. In contrast, remote sites such as Mauna Loa and Palau do not show significant seasonal variability. The seasonal variability from OMPS-NPP and N20 is consistent with FTIR observations.

We estimate the monthly uncertainties of OMPS-NPP/N20. At all sites, the uncertainty of OMPS-NPP (N20) is  $1.5$  ( $1.2$ )  $\times 10^{15}$  molecules cm<sup>-2</sup>. In clean sites, the total uncertainty for OMPS-NPP (N20) is  $0.7$  ( $0.8$ )  $\times 10^{15}$  molecules cm<sup>-2</sup>, corresponding to relative uncertainty of 32 (30)%. In the case of HCHO VCDs >  $4.0 \times 10^{15}$  molecules cm<sup>-2</sup>, however, the relative uncertainty of HCHO VCDs for OMPS-NPP (N20) decreases to 31 (18)%.

The bias correction is applied using constant and proportional biases for the sites with HCHO VCDs >  $4.0 \times 10^{15}$  molecules cm<sup>-2</sup>. After the correction, the relative uncertainty for OMPS-NPP is the same as that before the correction, but the bias improves from  $-15\%$  to  $-3\%$ . For OMPS-N20, the bias correction has no effects on the reduction of the bias and increases only total uncertainty arising from the correction.

We provide the bias and total uncertainty using FTIR observations. However, because FTIR observations are not true values, additional bias and uncertainty could remain. Also, the estimated bias and uncertainty are based on the monthly means at the horizontal grid of  $0.5^\circ$  and the spatial sampling of  $\pm 3$  hr. The bias and uncertainty provided in this study are lower limits for the given conditions and sites and need to be used carefully when applying them to further studies. Also, validation results need to be regularly reported to track the performance of OMPS-NPP/N20 HCHO products.

#### Acknowledgments

This study was supported by NASA's Making Earth System Data Records for Use in Research Environments (80NSSC18M0091), NASA The Science of Terra, Aqua and Suomi NPP (80NSSC18K0691), and NOAA's Climate Program Office's Atmospheric Chemistry, Carbon Cycle, and Climate Program (NA18OAR4310108). Computations in this paper were conducted at the Smithsonian High Performance Cluster (SI/HPC), Smithsonian Institution (<https://doi.org/10.25572/SI/HPC>). This study was supported by the research grant of the University of Suwon, 2022. Research at the University of Bremen has been supported by the BMBF (German Ministry of Research and Education) in

#### Data Availability Statement

The OMPS HCHO products from Suomi NPP (González Abad, 2022b) and NOAA-20 (González Abad, 2022a) are available at the NASA GES DISC. NDACC FTIR raw data are available at the website (NDACC, 2023) for most sites. Please see the NDACC data use agreement before the data are used (<https://ndacc.larc.nasa.gov/data/use-agreement>). Comparable pairs between OMPS and FTIR observations used in this study are available at the Harvard Dataverse (Kwon, 2022).

#### References

- Amador-Muñoz, O., Villalobos-Pietrini, R., Miranda, J., & Vera-Avila, L. E. (2011). Organic compounds of PM2.5 in Mexico Valley: Spatial and temporal patterns, behavior and sources. *Science of the Total Environment*, *409*(8), 1453–1465. <https://doi.org/10.1016/j.scitotenv.2010.11.026>
- Bak, J., Baek, K. H., Kim, J. H., Liu, X., Kim, J., & Chance, K. (2019). Cross-evaluation of GEMS tropospheric ozone retrieval performance using OMI data and the use of an ozonesonde dataset over East Asia for validation. *Atmospheric Measurement Techniques*, *12*(9), 5201–5215. <https://doi.org/10.5194/amt-12-5201-2019>

the project ROMIC-II subproject TroStra (01LG1904A). We thank the AWI Potsdam and the Impres GmbH, Bremen, for logistical and technical support in Palau. We thank the Coral Research foundation (CRRF) and the PCC Palau for support in conducting the measurements. We also thank the Senate of Bremen for partial support. We are grateful to T. Blumenstock, F. Hase, and M. Schneider as the PI of Kiruna, Karlsruhe, and Izaña stations, respectively. The NDACC stations at Bremen, Izaña, Karlsruhe, Kiruna, Paramaribo, and Zugspitze have been supported by the German Bundesministerium für Wirtschaft und Energie (BMWi) via DLR under Grants 50EE1711A, B, and D. The FTIR monitoring program at Jungfraujoch was primarily supported by the F.R.S.—FNRS (Brussels, Belgium) and the GAW-CH program of MeteoSwiss (Zürich, Switzerland). FTIR operations of Rikubetsu and Tsukuba sites are supported in part by the GOSAT series project. The NDACC site at as parts of the joint research program of the Institute for Space-Earth Environmental Research (ISEE), Nagoya University. Toronto measurements were made at the University of Toronto Atmospheric Observatory, which has received support from CFCAS, ABB Bomeh, CFI, CSA, ECCS, NSERC, ORDCF, PREA, and the University of Toronto. The Paris TCCON site has received funding from Sorbonne Université, the French Research Center CNRS, the French Space Agency CNES, and Région Île-de-France. We are grateful to N. Kumps and C. Hermans from BIRA-IASB and J.-M. Metzger and V. Duflot from LACy/UMR8105 and OSU-R/UMS3365—Université de La Réunion for supporting the FTIR measurements at the St Denis and Maito stations at La Réunion. We thank Pucai Wang and Weidong Nan (IAP/CAS) for providing the FTIR measurements at Xianghe. We thank C. A. B. Aquino and L. Gatti for helping to the Porto Velho measurements. FTIR measurements in Mexico were supported by Alejandro Bezanilla, César Guarín, and Miguel A. Robles and partly financed by UNAM with Grant DGAPA-PAPIIT IN111521.

- Bak, J., Liu, X., Kim, J. H., Haffner, D. P., Chance, K., Yang, K., & Sun, K. (2017). Characterization and correction of OMPS nadir mapper measurements for ozone profile retrievals. *Atmospheric Measurement Techniques*, *10*(11), 4373–4388. <https://doi.org/10.5194/amt-10-4373-2017>
- Behrens, L. K., Hilboll, A., Richter, A., Peters, E., Alvarado, L. M. A., Kalisz Hedegaard, A. B., et al. (2019). Detection of outflow of formaldehyde and glyoxal from the African continent to the Atlantic Ocean with a MAX-DOAS instrument. *Atmospheric Chemistry and Physics*, *19*(15), 10257–10278. <https://doi.org/10.5194/acp-19-10257-2019>
- Cao, H., Fu, T. M., Zhang, L., Henze, D. K., Miller, C. C., Lerot, C., et al. (2018). Adjoint inversion of Chinese non-methane volatile organic compound emissions using space-based observations of formaldehyde and glyoxal. *Atmospheric Chemistry and Physics*, *18*(20), 15017–15046. <https://doi.org/10.5194/acp-18-15017-2018>
- Chance, K., Palmer, P. I., Spurr, R. J. D., Martin, R. V., Kurosu, T. P., & Jacob, D. J. (2000). Satellite observations of formaldehyde over North America from GOME. *Geophysical Research Letters*, *27*(21), 3461–3464. <https://doi.org/10.1029/2000GL011857>
- Choi, J., Henze, D. K., Cao, H., Nowlan, C. R., González Abad, G., Kwon, H.-A., et al. (2022). An inversion framework for optimizing non-methane VOC emissions using remote sensing and airborne observations in Northeast Asia during the KORUS-AQ field campaign. *Journal of Geophysical Research: Atmospheres*, *127*, e2021JD035844. <https://doi.org/10.1029/2021JD035844>
- De Mazière, M., Thompson, A. M., Kurylo, M. J., Wild, J. D., Bernhard, G., Blumenstock, T., et al. (2018). The Network for the Detection of Atmospheric Composition Change (NDACC): History, status and perspectives. *Atmospheric Chemistry and Physics*, *18*(7), 4935–4964. <https://doi.org/10.5194/acp-18-4935-2018>
- De Smedt, I., Müller, J.-F., Stavrou, T., van der A, R., Eskes, H., & Van Roozendael, M. (2008). Twelve years of global observations of formaldehyde in the troposphere using GOME and SCIAMACHY sensors. *Atmospheric Chemistry and Physics*, *8*(16), 4947–4963. <https://doi.org/10.5194/acp-8-4947-2008>
- De Smedt, I., Pinardi, G., Vigouroux, C., Compernelle, S., Bais, A., Benavent, N., et al. (2021). Comparative assessment of TROPOMI and OMI formaldehyde observations and validation against MAX-DOAS network column measurements. *Atmospheric Chemistry and Physics*, *21*(16), 12561–12593. <https://doi.org/10.5194/acp-21-12561-2021>
- De Smedt, I., Stavrou, T., Hendrick, F., Danckaert, T., Vlemmix, T., Pinardi, G., et al. (2015). Diurnal, seasonal and long-term variations of global formaldehyde columns inferred from combined OMI and GOME-2 observations. *Atmospheric Chemistry and Physics*, *15*(21), 12519–12545. <https://doi.org/10.5194/acp-15-12519-2015>
- De Smedt, I., Theys, N., Yu, H., Danckaert, T., Lerot, C., Compernelle, S., et al. (2018). Algorithm theoretical baseline for formaldehyde retrievals from S5P TROPOMI and from the QA4ECV project. *Atmospheric Measurement Techniques*, *11*(4), 2395–2426. <https://doi.org/10.5194/amt-11-2395-2018>
- De Smedt, I., Van Roozendael, M., Stavrou, T., Müller, J. F., Lerot, C., Theys, N., et al. (2012). Improved retrieval of global tropospheric formaldehyde columns from GOME-2/MetOp-A addressing noise reduction and instrumental degradation issues. *Atmospheric Measurement Techniques*, *5*(11), 2933–2949. <https://doi.org/10.5194/amt-5-2933-2012>
- Franco, B., Marais, E. A., Bovy, B., Bader, W., Lejeune, B., Roland, G., et al. (2016). Diurnal cycle and multi-decadal trend of formaldehyde in the remote atmosphere near 46°N. *Atmospheric Chemistry and Physics*, *16*(6), 4171–4189. <https://doi.org/10.5194/acp-16-4171-2016>
- Fried, A., Walega, J., Weibring, P., Richter, D., Simpson, J. J., Blake, D. R., et al. (2020). Airborne formaldehyde and volatile organic compound measurements over the Daesan petrochemical complex on Korea's northwest coast during the Korea–United States Air Quality study: Estimation of emission fluxes and effects on air quality. *Elementa: Science of the Anthropocene*, *8*(1), 121. <https://doi.org/10.1525/elementa.2020.121>
- Gatz, D. F., & Smith, L. (1995). The standard error of a weighted mean concentration—I. Bootstrapping vs other methods. *Atmospheric Environment*, *29*(11), 1185–1193. [https://doi.org/10.1016/1352-2310\(94\)00210-c](https://doi.org/10.1016/1352-2310(94)00210-c)
- Go, S., Kim, J., Mok, J., Irie, H., Yoon, J., Torres, O., et al. (2020). Ground-based retrievals of aerosol column absorption in the UV spectral region and their implications for GEMS measurements. *Remote Sensing of Environment*, *245*, 111759. <https://doi.org/10.1016/j.rse.2020.111759>
- González Abad, G. (2022a). OMPS-N20 L2 NM formaldehyde (HCHO) total column swath orbital V1 [Dataset]. Goddard Earth Sciences Data and Information Services Center (GES DISC). <https://doi.org/10.5067/CIYXT9A4I2F4>
- González Abad, G. (2022b). OMPS-NPP L2 NM Formaldehyde (HCHO) Total Column swath orbital V1 [Dataset]. Goddard Earth Sciences Data and Information Services Center (GES DISC). <https://doi.org/10.5067/IIM1GHT07QA8>
- González Abad, G., Liu, X., Chance, K., Wang, H., Kurosu, T., & Suleiman, R. (2015). Updated Smithsonian Astrophysical Observatory Ozone Monitoring Instrument (SAO OMI) formaldehyde retrieval. *Atmospheric Measurement Techniques*, *8*(1), 19–32. <https://doi.org/10.5194/amt-8-19-2015>
- González Abad, G., Vasilkov, A., Seftor, C., Liu, X., & Chance, K. (2016). Smithsonian Astrophysical Observatory Ozone Mapping and Profiler Suite (SAO OMPS) formaldehyde retrieval. *Atmospheric Measurement Techniques*, *9*(7), 2797–2812. <https://doi.org/10.5194/amt-9-2797-2016>
- Gonzalez-Alonso, L., Val Martin, M., & Kahn, R. A. (2019). Biomass-burning smoke heights over the Amazon observed from space. *Atmospheric Chemistry and Physics*, *19*(3), 1685–1702. <https://doi.org/10.5194/acp-19-1685-2019>
- Hase, F., Hannigan, J. W., Coffey, M. T., Goldman, A., Höpfer, M., Jones, N. B., et al. (2004). Intercomparison of retrieval codes used for the analysis of high-resolution, ground-based FTIR measurements. *Journal of Quantitative Spectroscopy and Radiative Transfer*, *87*(1), 25–52. <https://doi.org/10.1016/j.jqsrt.2003.12.008>
- Kaiser, J., Jacob, D. J., Zhu, L., Travis, K. R., Fisher, J. A., González Abad, G., et al. (2018). High-resolution inversion of OMI formaldehyde columns to quantify isoprene emission on ecosystem-relevant scales: Application to the southeast US. *Atmospheric Chemistry and Physics*, *18*(8), 5483–5497. <https://doi.org/10.5194/acp-18-5483-2018>
- Kang, M., Ahn, M., Liu, X., Jeong, U., & Kim, J. (2020). Spectral calibration algorithm for the Geostationary Environment Monitoring Spectrometer (GEMS). Preprints.
- Kang, M., Ahn, M. H., Ko, D. H., Kim, J., Nicks, D., Eo, M., et al. (2022). Characteristics of the spectral response function of Geostationary Environment Monitoring Spectrometer analyzed by ground and in-orbit measurements. *IEEE Transactions on Geoscience and Remote Sensing*, *60*, 1–16. <https://doi.org/10.1109/tgrs.2021.3091677>
- Kim, G., Choi, Y.-S., Park, S. S., & Kim, J. (2021). Effect of solar zenith angle on satellite cloud retrievals based on O<sub>2</sub>–O<sub>2</sub> absorption band. *International Journal of Remote Sensing*, *42*(11), 4224–4240. <https://doi.org/10.1080/01431161.2021.1890267>
- Kim, J., Jeong, U., Ahn, M.-H., Kim, J. H., Park, R. J., Lee, H., et al. (2020). New era of air quality monitoring from space: Geostationary Environment Monitoring Spectrometer (GEMS). *Bulletin of the American Meteorological Society*, *101*(1), E1–E22. <https://doi.org/10.1175/BAMS-D-18-0013.1>
- Kim, M., Kim, J., Torres, O., Ahn, C., Kim, W., Jeong, U., et al. (2018). Optimal estimation-based algorithm to retrieve aerosol optical properties for GEMS measurements over Asia. *Remote Sensing*, *10*(2), 162. <https://doi.org/10.3390/rs10020162>
- Kramarova, N. A., Nash, E. R., Newman, P. A., Bhartia, P. K., McPeters, R. D., Rault, D. F., et al. (2014). Measuring the Antarctic ozone hole with the new Ozone Mapping and Profiler Suite (OMPS). *Atmospheric Chemistry and Physics*, *14*(5), 2353–2361. <https://doi.org/10.5194/acp-14-2353-2014>

- Kwon, H.-A. (2022). Comparable data of OMPS and FTIR formaldehyde observations for the validation of OMPS formaldehyde products [Dataset]. Harvard Dataverse. <https://doi.org/10.7910/DVN/MJC7PD>
- Kwon, H.-A., Park, R. J., González Abad, G., Chance, K., Kurosu, T. P., Kim, J., et al. (2019). Description of a formaldehyde retrieval algorithm for the Geostationary Environment Monitoring Spectrometer (GEMS). *Atmospheric Measurement Techniques*, *12*(7), 3551–3571. <https://doi.org/10.5194/amt-12-3551-2019>
- Kwon, H.-A., Park, R. J., Oak, Y. J., Nowlan, C. R., Janz, S. J., Kowalewski, M. G., et al. (2021). Top-down estimates of anthropogenic VOC emissions in South Korea using formaldehyde vertical column densities from aircraft during the KORUS-AQ campaign. *Elementa: Science of the Anthropocene*, *9*(1), 00109. <https://doi.org/10.1525/elementa.2021.00109>
- Langerock, B., De Mazière, M., Hendrick, F., Vigouroux, C., Desmet, F., Dils, B., & Niemeijer, S. (2015). Description of algorithms for co-locating and comparing gridded model data with remote-sensing observations. *Geoscientific Model Development*, *8*(3), 911–921. <https://doi.org/10.5194/gmd-8-911-2015>
- Li, C., Joiner, J., Krotkov, N. A., & Dunlap, L. (2015). A new method for global retrievals of HCHO total columns from the Suomi National Polar-orbiting Partnership Ozone Mapping and Profiler Suite. *Geophysical Research Letters*, *42*, 2515–2522. <https://doi.org/10.1002/2015GL063204>
- Li, C., Krotkov, N. A., Carn, S., Zhang, Y., Spurr, R. J. D., & Joiner, J. (2017). New-generation NASA Aura Ozone Monitoring Instrument (OMI) volcanic SO<sub>2</sub> dataset: Algorithm description, initial results, and continuation with the Suomi-NPP Ozone Mapping and Profiler Suite (OMPS). *Atmospheric Measurement Techniques*, *10*(2), 445–458. <https://doi.org/10.5194/amt-10-445-2017>
- Liao, J., Hanisco, T. F., Wolfe, G. M., St. Clair, J., Jimenez, J. L., Campuzano-Jost, P., et al. (2019). Towards a satellite formaldehyde—In situ hybrid estimate for organic aerosol abundance. *Atmospheric Chemistry and Physics*, *19*(5), 2765–2785. <https://doi.org/10.5194/acp-19-2765-2019>
- Malhi, Y., Roberts, J. T., Betts Richard, A., Killeen Timothy, J., Li, W., & Nobre Carlos, A. (2008). Climate change, deforestation, and the fate of the Amazon. *Science*, *319*(5860), 169–172. <https://doi.org/10.1126/science.1146961>
- Marais, E. A., Jacob, D. J., Jimenez, J. L., Campuzano-Jost, P., Day, D. A., Hu, W., et al. (2016). Aqueous-phase mechanism for secondary organic aerosol formation from isoprene: Application to the southeast United States and co-benefit of SO<sub>2</sub> emission controls. *Atmospheric Chemistry and Physics*, *16*(3), 1603–1618. <https://doi.org/10.5194/acp-16-1603-2016>
- NDACC. (2023). Network for the Detection of Atmospheric Composition Change (NDACC) Public Data Access [Dataset]. National Aeronautics and Space Administration (NASA). Retrieved from <https://www-air.larc.nasa.gov/missions/ndacc/data.html>
- Nowlan, C. R., González Abad, G., Kwon, H.-A., Ayazpour, Z., Chan Miller, C., Chance, K., et al. (2022). Global formaldehyde products from the Ozone Mapping and Profiler Suite (OMPS) nadir mappers on Suomi NPP and NOAA-20. *Earth and Space Science Open Archive*, *54*. <https://doi.org/10.1002/essoar.10512639.1>
- Nowlan, C. R., Liu, X., Janz, S. J., Kowalewski, M. G., Chance, K., Follette-Cook, M. B., et al. (2018). Nitrogen dioxide and formaldehyde measurements from the GEOstationary Coastal and Air Pollution Events (GEO-CAPE) airborne simulator over Houston, Texas. *Atmospheric Measurement Techniques*, *11*(11), 5941–5964. <https://doi.org/10.5194/amt-11-5941-2018>
- Park, J., Choi, W., Lee, H.-M., Park, R. J., Kim, S.-Y., Yu, J.-A., et al. (2021). Effect of error in SO<sub>2</sub> slant column density on the accuracy of SO<sub>2</sub> transport flow rate estimates based on GEMS synthetic radiances. *Remote Sensing*, *13*(15), 3047. <https://doi.org/10.3390/rs13153047>
- Rivera Cárdenas, C., Guafín, C., Stremme, W., Friedrich, M. M., Bezanilla, A., Rivera Ramos, D., et al. (2021). Formaldehyde total column densities over Mexico city: Comparison between multi-axis differential optical absorption spectroscopy and solar-absorption Fourier Transform Infrared measurements. *Atmospheric Measurement Techniques*, *14*(1), 595–613. <https://doi.org/10.5194/amt-14-595-2021>
- Rodgers, C. D., & Connor, B. J. (2003). Intercomparison of remote sounding instruments. *Journal of Geophysical Research*, *108*(D3), 4116. <https://doi.org/10.1029/2002JD002299>
- Schroeder, J. R., Crawford, J. H., Fried, A., Walega, J., Weinheimer, A., Wisthaler, A., et al. (2017). New insights into the column CH<sub>2</sub>O/NO<sub>2</sub> ratio as an indicator of near-surface ozone sensitivity. *Journal of Geophysical Research: Atmospheres*, *122*, 8885–8907. <https://doi.org/10.1002/2017JD026781>
- Souri, A. H., Chance, K., Bak, J., Nowlan, C. R., González Abad, G., Jung, Y., et al. (2021). Unraveling pathways of elevated ozone induced by the 2020 lockdown in Europe by an observationally constrained regional model using TROPOMI. *Atmospheric Chemistry and Physics*, *21*(24), 18227–18245. <https://doi.org/10.5194/acp-21-18227-2021>
- Souri, A. H., Nowlan, C. R., González Abad, G., Zhu, L., Blake, D. R., Fried, A., et al. (2020). An inversion of NO<sub>x</sub> and non-methane volatile organic compound (NMVOC) emissions using satellite observations during the KORUS-AQ campaign and implications for surface ozone over East Asia. *Atmospheric Chemistry and Physics*, *20*(16), 9837–9854. <https://doi.org/10.5194/acp-20-9837-2020>
- Spurr, R., & Christi, M. (2019). The LIDORT and VLIDORT linearized scalar and vector discrete ordinate radiative transfer models: Updates in the last 10 years. In A. Kokhanovsky (Ed.), *Springer series in light scattering: Volume 3: Radiative transfer and light scattering* (pp. 1–62). Springer International Publishing.
- Stavrakou, T., Müller, J. F., Bauwens, M., De Smedt, I., Van Roozendaal, M., De Mazière, M., et al. (2015). How consistent are top-down hydrocarbon emissions based on formaldehyde observations from GOME-2 and OMI? *Atmospheric Chemistry and Physics*, *15*(20), 11861–11884. <https://doi.org/10.5194/acp-15-11861-2015>
- Su, W., Liu, C., Hu, Q., Zhang, C., Liu, H., Xia, C., et al. (2022). First global observation of tropospheric formaldehyde from Chinese GaoFen-5 satellite: Locating source of volatile organic compounds. *Environmental Pollution*, *297*, 118691. <https://doi.org/10.1016/j.envpol.2021.118691>
- Torres, O. (2019). *OMPS-NPP L2 NM aerosol index swath orbital V2*. Goddard Earth Sciences Data and Information Services Center (GES DISC).
- Torres, O., Bhartia, P. K., Jethva, H., & Ahn, C. (2018). Impact of the Ozone Monitoring Instrument row anomaly on the long-term record of aerosol products. *Atmospheric Measurement Techniques*, *11*(5), 2701–2715. <https://doi.org/10.5194/amt-11-2701-2018>
- Travis, K. R., Judd, L. M., Crawford, J. H., Chen, G., Szykman, J., Whitehill, A., et al. (2022). Can column formaldehyde observations inform air quality monitoring strategies for ozone and related photochemical oxidants? *Journal of Geophysical Research: Atmospheres*, *127*, e2022JD036638. <https://doi.org/10.1029/2022JD036638>
- Vigouroux, C., Bauer Aquino, C. A., Bauwens, M., Becker, C., Blumenstock, T., De Mazière, M., et al. (2018). NDACC harmonized formaldehyde time series from 21 FTIR stations covering a wide range of column abundances. *Atmospheric Measurement Techniques*, *11*(9), 5049–5073. <https://doi.org/10.5194/amt-11-5049-2018>
- Vigouroux, C., Langerock, B., Bauer Aquino, C. A., Blumenstock, T., Cheng, Z., De Mazière, M., et al. (2020). TROPOMI–Sentinel-5 Precursor formaldehyde validation using an extensive network of ground-based Fourier-Transform Infrared stations. *Atmospheric Measurement Techniques*, *13*(7), 3751–3767. <https://doi.org/10.5194/amt-13-3751-2020>
- Wittrock, F., Richter, A., Oetjen, H., Burrows, J. P., Kanakidou, M., Myriokefalitakis, S., et al. (2006). Simultaneous global observations of glyoxal and formaldehyde from space. *Geophysical Research Letters*, *33*, L16804. <https://doi.org/10.1029/2006GL026310>



- Yang, K., Carn, S. A., Ge, C., Wang, J., & Dickerson, R. R. (2014). Advancing measurements of tropospheric NO<sub>2</sub> from space: New algorithm and first global results from OMPS. *Geophysical Research Letters*, *41*, 4777–4786. <https://doi.org/10.1002/2014GL060136>
- Yang, K., Dickerson, R. R., Carn, S. A., Ge, C., & Wang, J. (2013). First observations of SO<sub>2</sub> from the satellite Suomi NPP OMPS: Widespread air pollution events over China. *Geophysical Research Letters*, *40*, 4957–4962. <https://doi.org/10.1002/grl.50952>
- York, D., Evensen, N. M., Martínez, M. L., & De Basabe Delgado, J. (2004). Unified equations for the slope, intercept, and standard errors of the best straight line. *American Journal of Physics*, *72*(3), 367–375. <https://doi.org/10.1119/1.1632486>
- Zhu, L., González Abad, G., Nowlan, C. R., Chan Miller, C., Chance, K., Apel, E. C., et al. (2020). Validation of satellite formaldehyde (HCHO) retrievals using observations from 12 aircraft campaigns. *Atmospheric Chemistry and Physics*, *20*(20), 12329–12345. <https://doi.org/10.5194/acp-20-12329-2020>
- Zhu, L., Jacob, D. J., Kim, P. S., Fisher, J. A., Yu, K., Travis, K. R., et al. (2016). Observing atmospheric formaldehyde (HCHO) from space: Validation and intercomparison of six retrievals from four satellites (OMI, GOME2A, GOME2B, OMPS) with SEAC4RS aircraft observations over the southeast US. *Atmospheric Chemistry and Physics*, *16*(21), 13477–13490. <https://doi.org/10.5194/acp-16-13477-2016>
- Zoogman, P., Liu, X., Suleiman, R. M., Pennington, W. F., Flittner, D. E., Al-Saadi, J. A., et al. (2017). Tropospheric Emissions: Monitoring of Pollution (TEMPO). *Journal of Quantitative Spectroscopy and Radiative Transfer*, *186*, 17–39. <https://doi.org/10.1016/j.jqsrt.2016.05.008>